Adsorption of Al, O, Hf, Y, Pt, and S Atoms on α-Al₂O₃(0001)

Berit Hinnemann[†] and Emily A. Carter*,[‡]

Department of Mechanical and Aerospace Engineering and Department of Mechanical and Aerospace Engineering and Program in Applied and Computational Mathematics, Princeton University, Princeton, New Jersey 08544-5263

We use first-principles density functional theory to investigate adsorption of Al, O, Hf, Y, Pt, and S-atoms on the α-Al₂O₃(0001) surface. We identify stable adsorption sites and predict binding energies and structures. We find that Al, Hf, and Y preferentially adsorb on threefold-hollow sites, transfer electrons to the surface, and form ionic bonds to the three oxygen atoms. In contrast, the most stable adsorption site for Pt and S is ontop an oxygen atom, and we do not observe significant charge transfer. We find a binding order of S < Pt < O < Al ≪ Y < Hf, which reflects both the ease with which the early transition metals Hf and Y ionize, as well as the (nearly) closed-shell repulsions influencing the adsorption of O, Pt, and S. We use these results to rationalize some observations regarding the stability of thermal barrier coatings.

1. Introduction

Alumina is a technologically important oxide widely used in electronics, ceramics and catalysis[1−4] and it also plays a key role in thermal barrier coatings (TBCs).[5] TBCs protect jet engine parts from the extreme heat inside the engine; as a result, understanding their failure mechanisms and finding ways to prolong their lifetimes is of utmost importance.[6] In general, a TBC consists of (i) a ceramic topcoat, typically yttria-stabilized zirconia, (ii) a bond coat alloy based on NiAl, deposited onto the Ni-based superalloy engine component, and (iii) a thermally grown oxide (TGO) layer separating the ceramic topcoat from the bond coat.[7] For the TGO, α-Al₂O₃ is the oxide of choice, because it has the lowest oxygen diffusivity of all ceramics and therefore grows most slowly.[8,9] A thin layer of alumina is protective, but thickening of the TGO during high-temperature operation is one of the dominant causes of TBC failure; in practice a TGO can grow up to only 3−10 μm before it fails.[10] Thus, it is important to understand the growth mechanism of the TGO layer to work toward extending TBC lifetimes.

It is well-known that addition of reactive elements (REs) like Hf, Y, and Zr to the bond coat alloy slows down the growth of alumina. Experiments on NiAl oxidation indicate that the growth mechanism changes from outward diffusion of Al species in the undoped TGO to the (much slower) diffusion of O species in the RE-doped TGO layer.[11] Pint[12] has proposed that the REs segregate to the grain boundaries (GBs) of the polycrystalline TGO layer, where they block the movement of the Al species and change the rate-limiting growth step from diffusion of Al cations to diffusion of O anions. Even though this theory is consistent with experimental evidence, many atomistic aspects are unresolved. For example, even though there are indications that the diffusing species are charged,[13] their precise charge state is unknown and the specific pathways, energetics, and kinetics involved have yet to be characterized. Furthermore, the rate-limiting diffusion step remains controversial. Other oxidation

studies conclude that the growth of an alumina layer on FeCrAl alloys occurs via both inward oxygen diffusion and outward Al diffusion,[14−16] even though their relative contributions depend on the presence of reactive elements. The rate-limiting process for grain-boundary sliding in creep studies of alumina has suggested to be oxygen diffusion,[17] as predicted creep rates using GB and lattice diffusion of oxygen agree best with experimentally measured ones. However, as charge neutrality has to be preserved, both Al and O ion movement has to occur, and because O diffusion is slower than Al diffusion, it seems to be the rate-limiting process. Creep studies also find that dopant elements such as Y, La, and Lu hinder grain-boundary sliding (refs 17−22 and references therein). This effect has been interpreted to mean that the dopant atoms hinder oxygen diffusion along the GBs so that oxygen diffusion within the lattice becomes the rate-limiting process.[17] For example, Y appears to tie up oxygen in more covalent and perhaps stronger Y−O bonds (compared to ionic Al−O bonds), which has been suggested to strengthen GBs and reduce creep.[20,21,23] To summarize then, while there is substantial evidence for the role of reactive elements as inhibitors of TGO growth and creep, their precise mechanism is not entirely clear and the rate-limiting process for alumina scale growth cannot yet be uniquely identified. We hope that theoretical studies on very well-defined material structures, such as the present one, may shed light on this matter.

Another common dopant in TBCs with a very different role is Pt. Addition of 5 at. % Pt to the NiAl bond coat alloy is found to significantly improve overall TBC adhesion as well as corrosion resistance of the bond coat, but does not influence TGO growth or morphology.[24] By contrast, sulfur impurities in NiAl alloys are detrimental to interface adhesion and TBC lifetime.[10,25] However, Pt-containing NiAl alloys are tolerant to sulfur over a range of sulfur concentrations (1−7 ppma), i.e., Pt prevents delamination even in the presence of sulfur.[24] The origin of this S tolerance and improved adhesion and corrosion resistance is still under discussion.

As mentioned above, TBC failure correlates with growth of the TGO, and growth of the TGO is controlled by diffusion of

---

* Corresponding author. E-mail address: eac@princeton.edu.
† Department of Mechanical and Aerospace Engineering.
‡ Department of Mechanical and Aerospace Engineering and Program in Applied and Computational Mathematics.

the reactants Al and O. Diffusion of Al, O, and dopants occurs along GBs in polycrystalline α-Al₂O₃.[12,26,27] However, a multitude of different GBs with different orientations have been observed in α-Al₂O₃ (see e.g., refs 28−31 and references therein) and one can imagine that an even greater variety of GBs are present in the TBC layer under operating temperatures.

Therefore, as a first step and to characterize a baseline reference state, we investigate in this paper adsorption of Al, O, and various dopants and impurities (Hf, Y, Pt, and S) on the α-Al₂O₃(0001) surface. Predictions of diffusion kinetics for these adsorbates on α-Al₂O₃(0001) will be reported elsewhere.[32] A fundamental understanding of the behavior of these elements on the basal plane of alumina will serve as guidance for future studies on model GBs.

Some aspects of this study, especially the adsorption of Pt, are also highly relevant to catalysis, because transition metal particles on oxide supports are used as catalysts for a variety of reactions (e.g., CO hydrogenation, conversion of automobile exhaust, or refining of petroleum).[2] Even though the alumina used for catalyst support is usually γ-Al₂O₃, many model studies are carried out on α-Al₂O₃ or on thin films of transient phases of alumina on metal supports.[4,33−35] Furthermore, at high temperatures γ-Al₂O₃ undergoes a phase transition to α-Al₂O₃ and therefore studies on α-Al₂O₃ are relevant for catalysis at high temperatures (e.g., automotive catalysis).

We choose to study the α-Al₂O₃(0001) surface terminated by a single aluminum layer, because both experimental[36−39] and theoretical studies[40−50] have shown that it is the most stable surface termination under ultrahigh vacuum conditions. It is also by far the most-studied alumina surface[33,51,52] and therefore a good baseline system for our purposes. It also constitutes the surface forming the Σ3(0001) basal GB, which is frequently studied as a model GB because of its simplicity, even though it is not very common in polycrystalline alumina.[53,54] We note that under different environmental conditions the surface composition and structure of the α-Al₂O₃(0001) surface change,[55−59] but as we are interested in the adsorption on an alumina surface relevant to a GB interface in a TBC at high temperatures, we do not consider such composition and structural changes because the TBC GBs are buried interfaces with the composition of bulk α-Al₂O₃ (e.g., no hydroxyl groups will be present) and a variety of (ill-characterized) structures, such that choosing the basal plane as we have done here is an equally good (or bad) model to any other choice.

2. Computational Details

We use spin-polarized density functional theory (DFT)[60,61] as implemented in the Vienna Ab Initio Simulation Package (VASP).[62−64] The Kohn−Sham equations are solved using a plane-wave basis set and periodic boundary conditions. Electron exchange and correlation are described using the Perdew−Burke−Ernzerhof (PBE) version[65] of the generalized gradient approximation (GGA). The ion cores are described by projector-augmented wave (PAW) potentials[66] as implemented by Kresse and Joubert.[67] For the k-point sampling of the Brillouin zone, we use the Monkhorst-Pack scheme.[68]

We use a cutoff of 400 eV for the kinetic energy of the plane waves and 610 eV for the representation of the augmentation charges for all surface calculations, which converges the total energy up to 0.01 eV/atom. For the determination of the lattice parameters for bulk α-Al₂O₃ where we need to relax the unit cell vectors according to the stresses, a greater precision of the forces is required and we use a kinetic energy cutoff of 530 eV

(and again 610 eV for the representation of the augmentation charges). We use Gaussian smearing with a smearing width of 0.01 eV, which gives energies that differ less than 0.1 meV from values obtained using Blöchl's tetrahedron method.[69] We relax all atomic positions (no constraints, as discussed below in detail) according to their forces using a conjugate gradient algorithm, and the relaxation is stopped when the force on each atom is below 0.03 eV/Å. We have relaxed several structures until the forces were less than 0.01 eV/Å, but this did not lead to significant differences in total energies or structures.

2.1. Bulk α-Al₂O₃. The first step is to determine the lattice parameters of bulk α-Al₂O₃. Its space group is $R\bar{3}c$ (number 167), which can be represented either by a rhombohedral or a hexagonal unit cell.[70] We calculate the lattice parameters for the rhombohedral unit cell by uniformly varying the cell volume and fitting to the Murnaghan equation of state[71] and also by simultaneously relaxing both ions and cell volume and shape and for the hexagonal unit cell by relaxing the ions and the unit cell volume and shape. For the rhombohedral unit cell, we use 7 × 7 × 7 k-points and for the hexagonal cell 5 × 5 × 2 k-points, both of which are Γ-point-centered and have been tested to be converged to <0.001 eV/atom. The unit cell parameters determined from the two different approaches are virtually identical (difference less than 0.003 Å). For the rhombohedral unit cell, we find the lattice parameters $a = 5.179$ Å and $\alpha = 55.33°$ and the internal parameters $u_{rh} = 0.352$ and $v_{rh} = 0.556$. These parameters translate to the hexagonal cell parameters as $a = 4.809$ Å and $c = 13.115$ Å and the internal parameters $u = 0.352$ and $v = 0.306$. These values compare well to the experimental lattice constants $a = 4.760$ Å, $c = 12.989$ Å, $u = 0.352$, and $v = 0.306$[70] with deviations of 1%. The bulk modulus and its pressure derivative have been calculated from the Murnaghan equation of state as $B_0 = 230.4$ GPa and $B'_0 = 4.069$, respectively; and these also compare fairly well to experimental values of $B_0 = 254$ GPa and $B'_0 = 4.275$ listed in ref 72 with deviations of 9 and 7%, respectively.

Alumina has a direct band gap at the Γ-point, which experimentally has been determined to be 8.8 eV.[73] We calculate this band gap to be 6.2 eV, exhibiting the usual underestimation of band gaps by DFT and agreeing with results by other authors.[74]

The cohesive energy has been calculated with a kinetic energy cutoff of 400 eV and is found to be 31.2 eV per mole of alumina, which compares well to the experimental value of 32 eV (calculated from formation enthalpies at 298 K[75]). The cohesive energy is obtained as

$$E_{coh,Al_2O_3} = \frac{1}{6} E_{hex,Al_2O_3}^{tot} - (2E_{Al}^{tot} + 3E_O^{tot})$$

where $E_{hex,Al_2O_3}^{tot}$ is the total energy of one hexagonal unit cell of α-Al₂O₃, E_{Al}^{tot} is the total energy of one isolated Al atom in the gas phase, and E_O^{tot} is the total energy of one isolated O atom in the gas phase. The calculations on the isolated atoms are done as described below.

2.2. α-Al₂O₃(0001) Surface. Figure 1 displays the α-Al₂O₃(0001) surface with a termination of half an alumina layer considered here (the terminating half-layer can best be seen in the structure to the right at the bottom layer). We use a vacuum layer of 14 Å between slabs, which we have tested to be sufficient so that the alumina slab is truly isolated from its periodic images. For the initial relaxation of the structures, we use the real-space evaluation of the PAW projection operators,[76] but we subsequently refine all structures using the more accurate reciprocal-space evaluation. This is especially im-
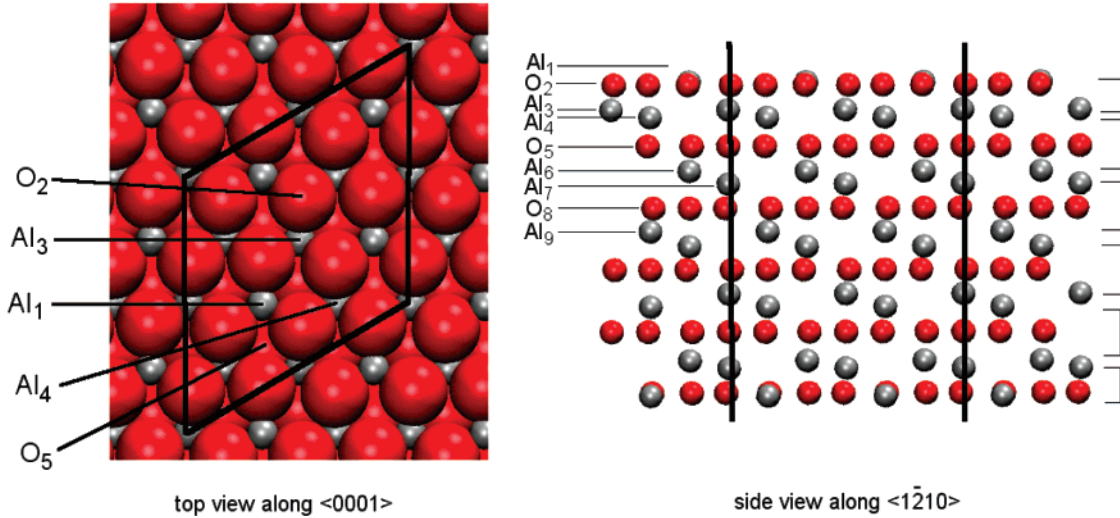
Figure 1. Top view (left) and side view (right) of our model of the α-Al$_2$O$_3$(0001) surface. The relaxed structure is shown. The top view shows the 2 × 2 unit cell and the labeling of the five high-symmetry adsorption sites. The side view shows on the right the six stoichiometric layers and on the left the layer labeling used in Table 1. The two vertical solid lines mark the extension of the unit cell employed. The color code is red (oxygen) and silver (aluminum). In the picture on the left, the size of the ions is chosen according to their Shannon ionic radii,[89] reflecting the ionicity of α-Al$_2$O$_3$.

TABLE 1: Comparison of Predicted and Measured Changes of Atomic Interlayer Spacings upon Relaxation in Å and in % with Respect to the Unrelaxed Geometry (Only the Top Half of the Slab Is Displayed Here Due to Symmetry)

| | theory | | | | | | | experiment | |
	this work (Å)	this work (%)	Verdozzi et al.[50] (%)	Hass et al.[56] (%)	Alavi et al.[81] (%)	Ruberto et al.[79] (%)	Carrasco et al.[80] (%)	Guenard et al.[39] (%)	Ahn et al.[36] (%)
O layers	9		18	3	3	9	11		
XC functional	PBE/PAW		LDA/NCPP	PBE/NCPP	PW91/USPP	PW91/NCPP	PBE/PAW		
Al$_1$−O$_2$	−0.733	−86.4	−87.4	−98	−97	−85.5	−93.8	−51	63
O$_2$−Al$_3$	+0.034	+4.0	+3.1	+5	+2	+3.2	+6.1	+16	
Al$_3$−Al$_4$	−0.223	−45.4	−41.7	−48	−53	−45.4	−46.7	−29	
Al$_4$−O$_5$	+0.174	+20.5	+18.3	+21	−27	+19.8	+22.0	+20	
O$_5$−Al$_6$	+0.043	+5.0	+5.6			+4.8	+8.5		
Al$_6$−Al$_7$	−0.033	−6.8	−8.3			−7.1	−11.6		
Al$_7$−O$_8$	+0.011	+1.3	+1.1			+1.3	+2.2		
O$_8$−Al$_9$	−0.011	−1.3	−0.5			−0.8	+0.7		
Al$_9$−Al$_{10}$	+0.023	+4.6	+6.4			+3.0	+3.8		
Al$_{10}$−O$_{11}$	−0.010	−1.2	−0.6			−0.7	−3.2		
O$_{11}$−Al$_{12}$	−0.002	−0.2	+0.5			+0.2	+2.2		

TABLE 2: Adsorption Energies and Magnetic Moments for an Al Atom on the Al$_4$ Site for 2 × 2 Surface Slabs of Different Thicknesses (Indicated in Numbers of Stoichiometric Layers) and Constraints (The Values in Parentheses Have Been Calculated Using a Dipole Correction)

O layers	constraints	E_{ads} [eV]	magn moment [μB]
9	none	−2.33 (−2.31)	1 (1)
9	4 middle atomic layers O$_{11}$, Al$_{12}$, Al$_{13}$, O$_{14}$ fixed	−2.33 (−2.31)	1 (1)
6	none	−2.33 (−2.31)	1 (1)
6	4 middle atomic layers O$_8$, Al$_9$, Al$_{10}$, O$_{11}$ fixed	−2.29 (−2.27)	1 (1)
4	none	−2.35 (−2.33)	1 (1)
4	3 bottom atomic layers Al$_{10}$, O$_{11}$, Al$_{12}$ fixed	−5.46 (−5.61)	−0.07 (−0.07)

portant for the calculations of vibrational frequencies, as the reciprocal-space evaluation leads to significantly more accurate forces.

We calculate the surface energy for both the unrelaxed and the relaxed surface for 3−9 stoichiometric layers in the slab. A stoichiometric layer consists of one oxygen layer and two aluminum layers (Al−O$_3$−Al), as marked in Figure 1. We obtain

surface energies of 3.50 and 1.54 J/m² for the unrelaxed (i.e., bulk-terminated structure) and relaxed surface, respectively; these values are converged to within 0.01 J/m² for six stoichiometric (Al−O$_3$−Al) layers. As to convergence with respect to kinetic energy cutoff and k-point sampling, increasing the kinetic energy cutoff from 400 to 530 eV changes the surface energy less than 0.01 J/m² and increasing the k-point sampling from 4 × 4 × 2 to 8 × 8 × 4 for the bulk and from 4 × 4 × 1 to 8 × 8 × 1 for the surface changes the surface energy less than 0.01 J/m². A surface energy of 1.54 J/m² agrees well with results by other authors using a similar methodology.[77−80] An experimental estimate of the surface energy from calorimetry gives 1.69 J/m².[57] The decrease of ∼2 J/m² in surface energy upon structural relaxation is due to large atom movements in which the Al atoms of the first layer move about ∼0.73 Å (86%) inward (these are our results, but they agree with well with refs 50 and 78−81).

This large difference in surface energies for the relaxed and unrelaxed surface can be understood considering that α-Al$_2$O$_3$ is a very ionic oxide, and several studies[49,79,82] have shown that it can be viewed as composed of Al^{3+} cations and O$^{2−}$ anions. The large inward relaxation of the top Al atoms upon relaxation

TABLE 3: Adsorption Energies, Magnetic Moments, and Types of Adsorption Sites for Adsorption of 1/12 ML Al, O, Hf, Y, Pt, and S on α-Al$_2$O$_3$(0001)^a

		Adsorption site				
		Al$_1$	O$_2$	Al$_3$	Al$_4$	O$_5$
Al	E_{ads} [eV]	−0.90 (−0.88)	→ Al$_4$	→ Al$_4$	−2.33 (−2.31)	→ Al$_4$
	magn moment [μB]	1 (1)			1 (1)	
	type of state	HOSP			min	
O	E_{ads} [eV]	−1.75 (−1.74)	−2.18 (−2.18)	→ Al$_1$	→ Al$_1$	−0.43 (−0.43)
	magn moment [μB]	2 (2)	0 (0)			0 (0)
	type of state	min	min			min
Hf	E_{ads} [eV]	−0.74 (−0.71)	→ Al$_4$	−3.52 (−3.52)^b −3.30 (−3.30)^b	−4.28 (−4.27)	→ Al$_4$
	magn moment [μB]	2 (2)		0 (0)^b 2 (2)^b	0 (0)	
	type of state	min		min HOSP	min	
Y	E_{ads} [eV]	−0.70 (−0.67)	→ Al$_4$	−3.15 (−3.15)	−3.90 (−3.90)	→ Al$_4$
	magn moment [μB]	1 (1)		1 (1)	1 (1)	
	type of state	HOSP^c		min	min	
Pt	E_{ads} [eV]	−1.06 (−1.06)	−2.02 (−2.02)	→ O$_2$	→ O$_2$	−1.60 (−1.60)
	magn moment [μB]	0 (0)	0 (0)			0 (0)
	type of state	HOSP^c	min^c			min^c
S	E_{ads} [eV]	−1.05 (−1.05)	−1.78 (−1.78)	→ O$_2$	→ O$_2$	−1.06 (−1.03)
	magn moment [μB]	2 (2)	0 (0)			0 (0)
	type of state	HOSP	min			min

^{a} The values without parentheses are calculated without dipole correction, the values in parentheses are calculated with dipole correction. The type of state labels are min = minimum, TS = transition state, and HOSP = higher-order saddle point. Arrows indicate that the high-symmetry initial guess relaxed to a different (indicated) geometry. ^{b} For adsorption of Hf on the Al$_3$ site, we find two stable structures: one with an adsorption energy of −3.52 eV and a magnetic moment of 0 μ_B (local minimum) and a structure with adsorption energy of −3.30 eV and a magnetic moment of 2 μ_B (HOSP). ^{c} Frequencies also calculated with displacements of 0.03 and 0.05 Å to investigate whether small frequencies are real or imaginary.

of the surface is driven by charge redistribution; in the bulk positions, the surface Al ions have a less positive charge than the bulk Al ions.[49,50,77,82] This causes a decrease of the surface band gap and the appearance of a surface state 2 eV below the conduction band minimum. Upon structural relaxation, electron transfer occurs from Al to O and the surface state moves up by more than 4 eV to 2.7 eV above the conduction band minimum.[50] Also, we calculate that the Al−O distance, which is 1.87 Å in the bulk, decreases to 1.70 Å at the surface, which again agrees with similar studies.[77] Verdozzi et al.[50] showed that for the calculation of surface relaxations, a 9-layer slab is sufficient and yields similar results to an 18-layer slab. To validate our calculations, we list our results for the surface relaxations for a 9-layer slab in Table 1 together with results by other authors and experimental data. Our DFT results agree well with those obtained by other researchers using a similar methodology. However, the calculated relaxations, especially the ones in the first layer, are significantly larger that the experimentally observed ones. This is likely because of the presence of hydrogen in the experiment,[56] e.g., Ahn and Rabalais[36] observed that even at temperatures as high as 1100 °C, hydrogen atoms were still present on the surface.

2.3. Adsorption. We use a 2 × 2 unit cell to investigate the adsorption of Al, O, Hf, Y, Pt, and S on the surface. One adsorbate atom per 2 × 2 unit cell corresponds to a geometrical coverage of 1/12 ML ≈ 0.08 ML following the definition of Verdozzi et al.[50] who define a "geometric monolayer" as one metal atom per surface oxygen. We choose this coverage as it is a typical coverage of dopants at alumina GBs.[12] We investigate five different high-symmetry adsorption sites, which we name according to the atoms lying directly beneath the site

(following the nomenclature used by Hernández et al.[83]). Figure 1 displays the five different adsorption sites, Al$_1$, O$_2$, Al$_3$, Al$_4$ and O$_5$, in which the numbered subscript refers to the layer in which the atom resides. We remark that we use the underlying atom solely for naming of the site, and we do not expect interactions between the adsorbates and the atoms in the fourth or fifth layer. Also, we try to avoid any confusion between the O$_2$ site on the surface and the oxygen molecule O$_2$ by always denoting the gaseous oxygen molecule as O$_2$(gas).

As the single adatoms have a magnetic moment, which they may retain upon adsorption on the surface, we carry out all calculations spin-polarized and try different initial guesses for the magnetic moments for each adatom to find the lowest energy state. We position the adatoms above the surface at a suitable distance equal to sums of covalent radii and then relax all atoms. We give the adsorbate atom a very small displacement from the high-symmetry site, so that it does not get stuck in a metastable state due to symmetry constraints. We first perform a complete structural relaxation without correcting for the artificial interaction of the slab images due to dipole moments. Then, we perform a subsequent structural relaxation correcting energies and forces for the contributions of these dipole moments,[76] and we report both energies without dipole correction and with dipole correction.

We calculate the adsorption energy of adsorbate X as

$$E_{ads,X} = E^{tot}_{X/Al_2O_3} - (E^{tot}_{Al_2O_3} + E^{tot}_{X}) \qquad (1)$$

where E^{tot}_{X/Al_2O_3} is the total energy of the adsorbate−substrate system, $E^{tot}_{Al_2O_3}$ is the energy of the clean α-Al$_2$O$_3$ surface slab,

TABLE 4: Calculated Vibrational Frequencies (in cm^{-1}) Which Involve Significant Adsorbate Motion (at Least One Component of the Eigenvector >0.05 Å)[a]

	adsorption site					
	Al$_1$	O$_2$	Al$_3$	Al$_3$	Al$_4$	O$_5$
Al	41i (parallel) 41i (parallel) 142[c], 307[d]	→ Al$_4$	→ Al$_4$		180 (parallel) 206 (parallel) 222[e], 447[f]	→ Al$_4$
O	11[b] (parallel) 65[b] (parallel) 208[g],211[g], 635[h]	206 (parallel) 233[i], 281[i], 315[i] 550[i], 583[i], 707[i], 876[i]	→ Al$_1$		→ Al$_1$	203−903[j]
Hf	13[b] (parallel) 20[b] (parallel) 61[b,k] (perp)	→ Al$_4$	0 μ_B[b] 36i (parallel) 36i (parallel) 129[l]	2 μ_B 88 (parallel) 96 (parallel) 136[l]	92 (parallel) 105 (parallel) 125[l] (perp)	→ Al$_4$
Y	49i[b] (parallel) 41i[b] (parallel) 64[b,k] (perp)	→ Al$_4$	116 (parallel) 119 (parallel) 174[l] (perp)		121 (parallel) 126 (parallel) 178[l] (perp)	→ Al$_4$
Pt	25i[b] (parallel) 12i[b] (parallel) 67[k] (perp)	25[b] (parallel) 61[b,m] 111[b,m]	→ O$_2$		→ O$_2$	8[b,m] 55[b,m] 100[b,m]
S	76i[b] (parallel) 61i[b] (parallel) 163[n],367[o],371[o],383[o]	120 (parallel) 166[p], 244[p] 475[p], 706[p]	→ O$_2$		→ O$_2$	128[q], 141[q], 151[q] 222[m], 319[m], 380[m] 554[q]

[a] For most structures, there are two modes parallel and weakly coupled to the surface and other modes with movement perpendicular to the surface, whose qualitative characters are described in the footnotes. These results are intended only to give a qualitative feel as to how deep or shallow the local minima are. [b] Frequencies also calculated with displacements of 0.03 and 0.05 Å to verify whether small frequencies are real or imaginary. [c] Adsorbate motion along z-direction in-phase with underlying Al$_1$ atom. [d] Adsorbate motion along z-direction out-of-phase with underlying Al$_1$ atom. [e] Adsorbate motion along z-direction in-phase with underlying Al$_4$ atom and the three surrounding O$_2$ atoms. [f] Adsorbate motion along z-direction out-of-phase with underlying Al$_4$ atom and the three surrounding O$_2$ atoms. [g] Adsorbate motion along z-direction in-phase with underlying Al$_1$ atom. [h] Adsorbate motion along z-direction out-of-phase with underlying Al$_1$ atom. [i] Modes involving adsorbate motion (>0.05 Å) strongly coupled to underlying O$_2$(1) and coordinated Al$_1$(1) atoms (see Table 5 for structure) so that separation of adsorbate modes is not possible. [j] The O adsorbate is so strongly coupled to the surrounding atoms that it is involved significantly in many modes in a range of frequencies, which we indicate here. [k] Adsorbate motion along z-direction and only very weakly coupled to coordinated Al$_1$ atom. [l] Adsorbate motion along z-direction and only weakly coupled to coordinated O$_2$ atoms. [m] Adsorbate motion along y- and z-direction only weakly coupled to nearby O$_2$ and Al$_1$ atoms. [n] Adsorbate motion along z-axis in phase with underlying Al$_1$ atom and coupled to nearby O$_2$ atoms. [o] Adsorbate motion along z-axis in phase with underlying Al$_1$ atom and coupled to nearby O$_2$ atoms. [p] Adsorbate motion along y-and z-axis coupled to the nearby Al$_1$ and O$_2$ atoms. [q] We list all modes that involve adsorbate motion (>0.05 Å) and all modes that are strongly coupled to the surrounding Al$_1$, O$_2$, and Al$_3$ atoms.

and E_X^{tot} is the energy of the ground state isolated atom X with X = Al, O, Hf, Y, Pt, S.

We emphasize that we investigate the adsorption of neutral atoms on the surface so that the entire system is charge-neutral. Even though there are indications that the diffusing species in the TGO are charged,[13] their precise charge state is unclear. When they enter alumina, in the case of Al from the underlying bond coat alloy and in the case of O from gas-phase O$_2$ into the ceramic topcoat, the species are originally charge-neutral, but their charge state may change upon entering and diffusing within α-Al$_2$O$_3$. Thus, we investigate the adsorption of neutral atoms and will assess the amount of charge transfer upon adsorption by charge density difference and local density of states (LDOS) analysis.

2.4. Isolated Atoms. The calculations for the isolated atoms employed unit cells of at least 10 × 10 × 10 Å in size and we have tried cubic, tetragonal, and trigonal cells of different sizes to ensure that we obtain the correct ground state. For numerical consistency, we use the same kinetic energy cutoff (400 eV) and augmentation cutoff (610 eV) as for the surface calculations. We use either Gaussian smearing with widths of 0.01−0.0001 eV or fixed occupation numbers, and we check for each atom that there are no partial occupancies. For each atom, we analyze the resulting orbitals and check that the correct electronic ground state is obtained: ^{2}P (s^2p^1) for Al, ^{3}P (s^2p^4) for O, ^{3}F (s^2d^2) for Hf, ^{2}D (s^2d^1) for Y, ^{3}D (s^1d^9) for Pt, and ^{3}P (s^2p^4) for S; we have used these ground states for all calculations. We remark that spin-contamination in spin-polarized DFT produces only approximate ground states and that convergence of isolated atoms is generally problematic. However, our main conclusions

will be based on differences in adsorption energies between different adsorption sites in which the energies of the isolated atoms do not enter.

As Hf and Y are early transition metals, their semicore states may influence adsorption energies and other properties, and therefore we have carried out all calculations that include these elements using PAW potentials incorporating these states. For Hf, the PAW potential used results in explicit treatment of the $(5p)^6(6s)^2(5d)^2$ electron configuration, and the PAW potential for Y corresponds to an explicit treatment of the $(4s)^2(4p)^6$-$(5s)^2(4d)^1$ electron configuration.[76] We have calculated adsorption energies using two different PAW potentials for Hf with and without the 5p semicore states treated explicitly and we find energy differences less than 0.1 eV. Nevertheless, in this paper we report the values calculated including the semicore states.

2.5. Choice of Slab Thickness. Using a 9-layer slab for our adsorption calculations would be computationally intensive, and most computational studies employ thinner slabs. Moreover, different computational studies have imposed different constraints on the surface. The effect of the surface thickness and of constraints needs to be tested carefully. Here, we choose the adsorption energy of an Al atom as the quantity we test for convergence. As will be discussed in the following section, Al adsorbs preferentially on the Al$_4$ site (see Figure 1).

As shown in Table 1, atom relaxations due to creation of a surface only take place in the first three stoichiometric (Al−O$_3$−Al) layers, and relaxations in deeper layers are rather small (<5%). Therefore, as Verdozzi et al.[50] already pointed out, a 9-layer slab is sufficient for the accurate calculation of

TABLE 5: Structures for the Minimum Energy Adsorption Sites Both in Top and in Tilted Side View[a]
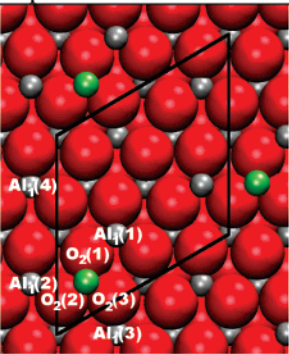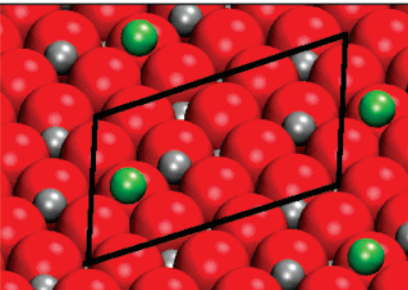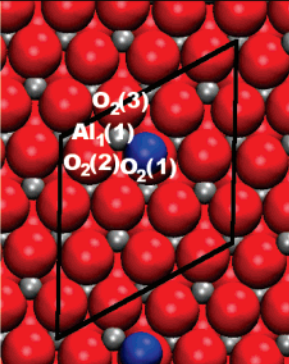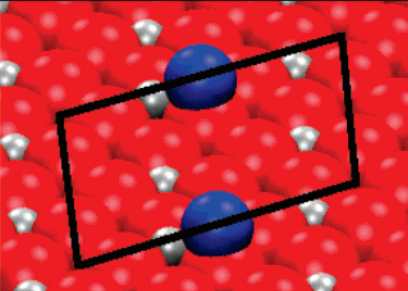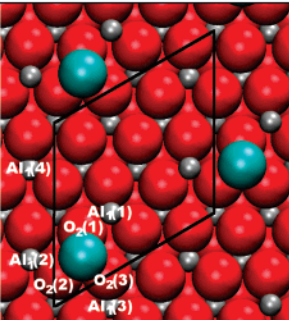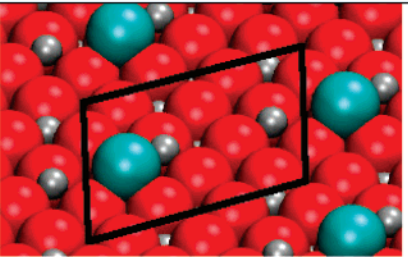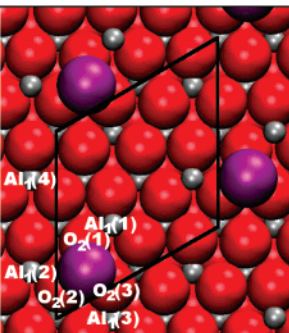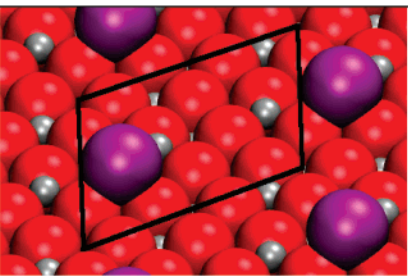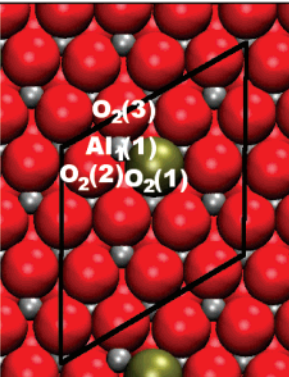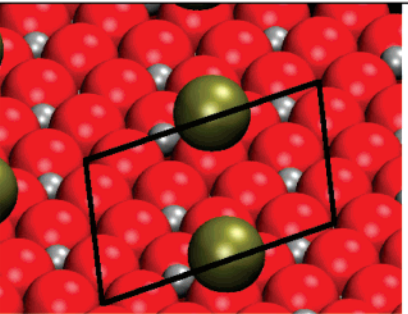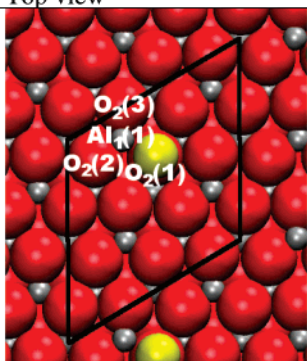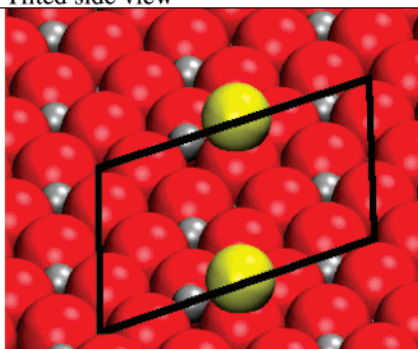
Adsorbate	Site	Top view	Tilted side view
Al[b]	Al$_4$		
O[c]	O$_2$		
Hf[d]	Al$_4$		
Y[e]	Al$_4$		
Pt[f]	O$_2$		

Al, O, Hf, Y, Pt, and S-Atoms on α-Al₂O₃(0001)

J. Phys. Chem. C, Vol. 111, No. 19, 2007 **7111**

TABLE 5: (Continued)

Adsorbate	Site	Top view	Tilted side view
S[g]	O₂		

[a] The unit cell has been drawn in black. The color code is red (oxygen), silver (aluminum). The aluminum and oxygen radii have been chosen according to their Shannon radii to reflect the ionicity of α-Al₂O₃. The atom labels are referred to in Table 6 and in the discussion in the text. Note that for better visibility the structures for O, Pt, and S are rotated about 120° compared to the other structures. [b] The Al adsorbate is displayed in light green for better visibility. It is displayed as the same size as the other Al ions although its electronic structure and therefore its "size" is different; see discussion in the text. [c] The O adsorbate is displayed in blue for better visibility. We have chosen to display it in a smaller size than the oxygen ions on the alumina surface for better visibility. Also, its electronic structure and therefore its "size" are different; see discussion in the text. [d] The Hf adsorbate is displayed in cyan and its size is chosen according to its atomic radius, although its size is different because of charge transfer; see discussion in the text. [e] The Y adsorbate is displayed in purple and its size is chosen according to its atomic radius, although its size is different because of charge transfer; see discussion in the text. [f] The Pt adsorbate is displayed in brown and its size is chosen according to its atomic radius. [g] The S adsorbate is displayed in yellow and its size is chosen according to its atomic radius, although its size is different because of charge transfer; see discussion in the text.

adsorption energies, and the middle layers of the slab should be unaffected by the adsorbate. It is shown in Table 2 that this is indeed the case. We obtain an adsorption energy of −2.33 eV (−2.31 eV including dipole correction) for an Al atom in the Al₄ site, and this energy is unaffected by keeping four middle atomic layers fixed at bulk values. For a slab consisting of six stoichiometric layers, we find that if we relax the whole slab, we get the same adsorption energy as for the 9-layer slab, whereas fixing the four middle atomic layers changes the adsorption energy by 0.02 eV. Thus, using a slab of six stoichiometric layers and relaxing all atoms gives reliable adsorption energies and we will use this approach in what follows.

Because several studies (e.g., refs 84−86) used surface slab models in which the bottom layer was kept fixed in bulk positions (an approach that is typically used for metal surfaces), we also test this approach using a 4-layer slab. By keeping the bottom layer fixed, we prevent the outermost Al ions on the bottom side of the slab from relaxing inward and thereby creating a large dipole moment (~1.3 eÅ). The force in the z-direction on the outermost Al ions on the side kept frozen is very large, ~6.4 eV/Å, and the total energy change for the bare surface (without adatoms) due to the dipole correction is 0.16 eV. By contrast, it is always <0.001 eV for the completely relaxed surfaces, as expected, because in this case the slab has mirror symmetry in the z-direction. As alumina is a very ionic solid with an estimated 60−90% ionicity,[79,87,88] fixing bottom layers of atoms in bulk positions artificially creates a large dipole moment, thereby changing the electronic structure and producing erroneous (see Table 2) adsorption energies (off by >3 eV) and adsorbate magnetic moments (off by 1 μ_B). We therefore always allow full relaxation of the atoms in these slab calculations.

2.6. Vibrational Frequencies. We analyze the vibrational frequencies of the adsorbates to be able to distinguish between minima, transition states (TS), and higher-order saddle points (HOSP). This is done via displacing by a short distance the adsorbate atom and all atoms within a 3 Å radius around it. We use central displacements, i.e., we displace each atom a

small positive and a small negative amount from its equilibrium position. From the finite differences of the forces produced by these displacements, one obtains a numerical estimate of the Hessian matrix and can find its eigenvalues (frequencies) and eigenvectors (eigenmodes). We generally use a displacement of 0.02 Å. We tested displacements of 0.01−0.05 Å and found that the frequencies generally change less than 10 cm⁻¹ over that range. One would ideally use as small a displacement as possible to stay in the harmonic region, but for too small a displacement the force differences might be dominated by noise, so we find 0.02 Å to be a good compromise. The analysis of the frequencies is carried out including the dipole correction, but we have tested that the results change only very slightly when the dipole correction is not used. For several structures with very small frequencies, it is difficult to distinguish between small real and small imaginary frequencies, as they are dominated by noise in the force differences. For these cases, we also calculated the vibrational frequencies for larger displacements of 0.03−0.07 Å. Even though by doing so one might probe the local potential surface beyond the harmonic region, the changes in forces will then be larger than their uncertainty. This then allows one to decide whether the small frequencies are real or imaginary. We performed this analysis for structures with frequencies <100 cm⁻¹, and these structures will be marked in the table as being analyzed in this way.

2.7. Charge Density Differences. Charge density differences $\Delta\rho$ are calculated via

$$\Delta\rho = \rho_{X/Al_2O_3} - (\rho_{Al_2O_3}^{frozen} + \rho_X^{frozen}) \quad (2)$$

where ρ_{X/Al_2O_3} is the electron density for the adsorbate−substrate system in its minimum-energy configuration, $\rho_{Al_2O_3}^{frozen}$ is the electron density of the surface which is kept frozen in the positions of the adsorbate−surface system, and ρ_X^{frozen} is the electron density of the isolated adatom at the same position as in the adsorbate−surface system. The charge density analysis is carried out including the dipole correction. In the electron

TABLE 6: Distances from the Adsorbates to Their Nearest Neighbors and Other Relevant Geometric Quantities for the Energetically Most Stable Site for Each Adsorbate[a]

adsorbate	site							
Al	Al$_4$	Al$_{ads}$−O$_2$(1)	Al$_{ads}$−O$_2$(2)	Al$_{ads}$−O$_2$(3)	O$_2$(1)−Al$_1$(1)	O$_2$(2)−Al$_1$(2)	O$_2$(3)−Al$_1$(3)	O−Al$_1$(4)[c]
distances [Å][b]		1.94	2.01	2.00	1.84	1.82	1.79	1.71
interlayer spacing[d,e] [Å]		Al$_{ads}$[f]	Al$_1$(1)	Al$_1$(2)	Al$_1$(3)	Al$_1$(4)		
		1.34	0.65	0.64	−0.39	0.16		
O	O$_2$	O$_{ads}$−O$_2$(1)	O$_{ads}$−Al$_1$(1)	Al$_1$(1)−O$_2$(1)	Al$_1$(1)−O$_2$(2)	Al$_1$(1)−O$_2$(3)		
distances [Å][b]		1.55	1.79	1.83	1.72	1.72		
interlayer spacing[d,e] [Å]		Al$_1$(1)						
		0.54						
Hf	Al$_4$	Hf$_{ads}$−O$_2$(1)	Hf$_{ads}$−O$_2$(2)	Hf$_{ads}$−O$_2$(3)	O$_2$(1)−Al$_1$(1)	O$_2$(2)−Al$_1$(2)	O$_2$(3)−Al$_1$(3)	O−Al$_1$(4)[c]
distances [Å][b]		1.98	2.20	2.07	2.06	1.89	1.82	1.71
interlayer spacing[d,e] [Å]		Hf$_{ads}$[g]	Al$_1$(1)	Al$_1$(2)	Al$_1$(3)	Al$_1$(4)		
		1.47	0.89	0.79	−0.53	0.13		
Y	Al$_4$	Y$_{ads}$−O$_2$(1)	Y$_{ads}$−O$_2$(2)	Y$_{ads}$−O$_2$(3)	O$_2$(1)−Al$_1$(1)	O$_2$(2)−Al$_1$(2)	O$_2$(3)−Al$_1$(3)	O−Al$_1$(4)[c]
distances [Å][b]		2.22	2.32	2.22	1.93	1.82	1.81	1.71
interlayer spacing[d,e] [Å]		Y$_{ads}$	Al$_1$(1)	Al$_1$(2)	Al$_1$(3)	Al$_1$(4)		
		1.69	0.79	0.61	−0.55	0.11		
Pt	O$_2$	Pt$_{ads}$−O$_2$(1)	Pt$_{ads}$−Al$_1$(1)	Al$_1$(1)−O$_2$(1)	Al$_1$(1)−O$_2$(2)	Al$_1$(1)−O$_2$(3)		
distances [Å][b]		2.03	2.36	1.84	1.72	1.73		
interlayer spacing[d,e] [Å]		Al$_1$(1)						
		0.55						
S	O$_2$	S$_{ads}$−O$_2$(1)	S$_{ads}$−Al$_1$(1)	Al$_1$(1)−O$_2$(1)	Al$_1$(1)−O$_2$(2)	Al$_1$(1)−O$_2$(3)		
distances [Å][b]		1.82	2.21	1.86	1.72	1.72		
interlayer spacing[d,e] [Å]		Al$_1$(1)						
		0.55						

[a] These quantities are obtained from structures which have been calculated using the dipole correction. For the labeling of atoms, see Table 5. [b] For comparison, the Al−O distance in bulk alumina is 1.88 Å, and on the clean surface it is 1.70 Å. [c] The distances of Al$_1$(4) to the three neighboring O atoms vary less than 0.005 Å, and therefore the average value is listed. [d] Calculated as the difference in the z-coordinate between the adsorbate atom and the average z-coordinate of the three neighboring O$_2$ atoms. [e] For comparison, the values for the clean surface is 0.116 Å, and for bulk alumina it is 0.848 Å. [f] Notice that O$_2$(3) is ∼0.1 Å higher than O$_2$(1) and O$_2$(2). [g] Notice that O$_2$(3) is ∼0.2 Å higher than O$_2$(1) and O$_2$(2).

density difference plots in Table 7, we show two isosurfaces at $\Delta\rho = -0.05$ e/Å^3 and $\Delta\rho = +0.05$ e/Å^3. The average (valence) electron density for α-Al$_2$O$_3$ in the bulk using the calculated unit cell parameters is $\rho = 144$e/262.67 Å^3 = 0.55 e/Å^3. The isosurfaces thus represent a change of $\Delta\rho/\rho = 9\%$, which is significant.

2.8. LDOS. We also analyze the LDOS for the adsorbate atoms and their nearest neighbors. For this analysis, we use Gaussian smearing with a width of 0.1 eV. This does not change the results but improves the visibility of the LDOS plots. To calculate the LDOS, one needs to choose the radii for the atoms in which the LDOS are analyzed. Here we choose the radii to

be the Wigner−Seitz radii from the PAW potentials, which enables us to use the quick projection scheme implemented in VASP.[76] For test cases, we have calculated the LDOS using atomic, covalent, and ionic radii (the latter as defined by Shannon[89]); only the absolute values but not the shape of the LDOS is changed (with the exception of Al for which the ionic radius is too small to obtain a LDOS significantly larger than noise). The LDOS analysis is carried out including the dipole correction.

We use the LDOS to get information about the charge state of the adsorbates. However, as the charge redistributions upon adsorption (Table 7) have complex shapes, simply integrating

TABLE 7: Charge Density Difference Plots for Adsorbates on the Minimum Energy Sites[a]
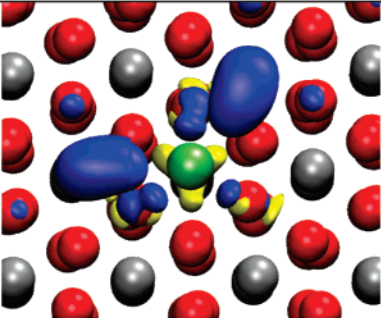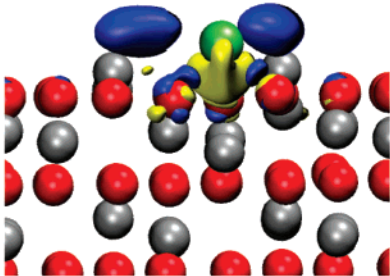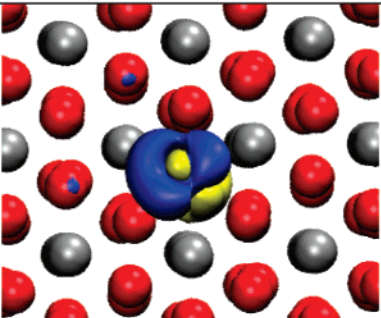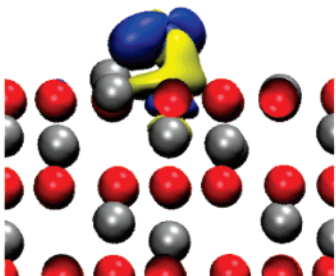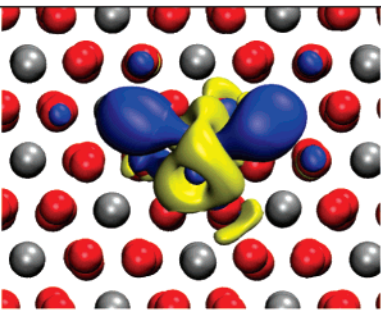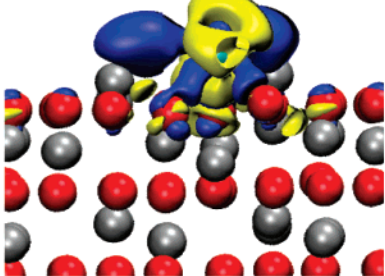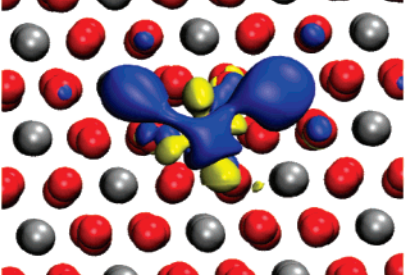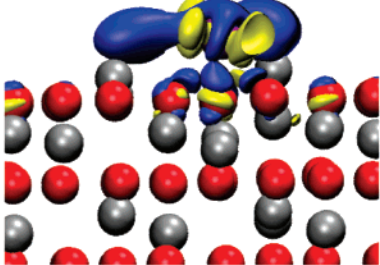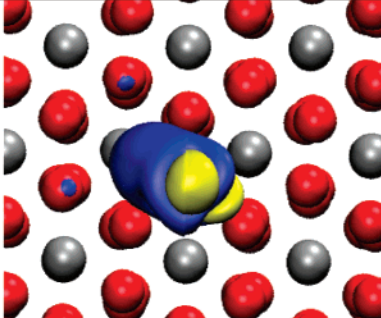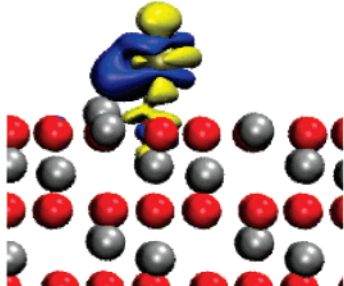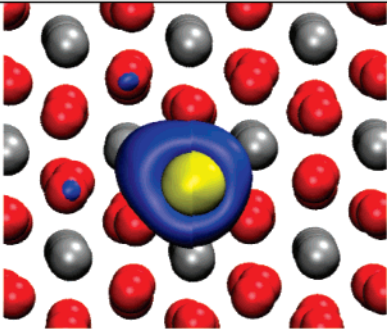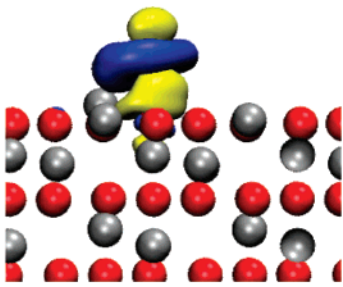
Adsorbate	Site	Charge density difference plot	
		Top view	Side view
Al	Al$_4$		
O	O$_2$		
Hf[a]	Al$_4$		
Y[a]	Al$_4$		
Pt	O$_2$		

TABLE 7: (Continued)

Adsorbate	Site	Charge density difference plot	
		Top view	Side view
S	O_2		

[a] The contour values are -0.05 e/$Å^3$ (yellow) and 0.05 e/$Å^3$ (blue) in which the blue surface corresponds to an accumulation of electrons and the yellow surface corresponds to electron depletion. [b] In the side view, the yellow isosurface with the isovalue of -0.05 e/$Å^3$ appears to be cut off. Only one unit cell in the direction into the paper is shown, and as a small part of the isosurface extends into the next unit cell it appears to be cut off.

the charge density within a certain radius for each atom would give a poor estimate of the local charge. Thus, we restrict ourselves to qualitative conclusions based on the LDOS shapes. More sophisticated analysis of the charge density distribution is outside the scope of this paper.

All figures showing atomic structures and charge density difference plots have been generated using the Visual Molecular Dynamics (VMD) program.[90]

3. Results

In the following, we present results for the adsorption of Al, O, Hf, Y, Pt, and S on the Al_1, O_2, Al_3, Al_4, and O_5 sites. The adsorption energies are listed in Table 3, and the vibrational frequencies are given in Table 4. The structures are shown in Table 5 and the bond lengths and other relevant distances are given in Table 6. For the electronic analysis, charge density difference plots are shown in Table 7 and local density of states plots are shown in Figures 2−7.

3.1. Al on α-Al_2O_3. For the adsorption of Al, relaxation of the starting structures on the five different adsites leads only to two stable structures. The only local minimum and most stable adsorption site is the Al_4 site, which has an adsorption energy of -2.33 eV (-2.31 eV with dipole correction). This result can be understood intuitively, since it corresponds to the site in which Al would adsorb for the α-Al_2O_3 to epitaxially grow further.

Adsorption on the Al_1 site leads to a structure where the Al atom is located 2.8 Å above the Al_1 atom, and correspondingly its interaction with the surface is rather weak and its adsorption energy is small with -0.90 eV (-0.88 eV with dipole correction). Furthermore, vibrational calculations show that this state is a higher-order saddle point and therefore we do not consider it further.

Vibrational calculations, as presented in Table 4, show that the Al_4 site indeed is a local minimum and the vibrational frequencies are high enough to allow for this unambiguous identification. We find frequencies of $\sim$180 and $\sim$206 cm^{-1} for vibrational movement parallel to the surface; for vibrations perpendicular to the surface, we find a frequency of $\sim$222 cm^{-1} for in-phase movement of the Al adsorbate and the underlying Al_4 atom and the three surrounding O_2 atoms and $\sim$447 cm^{-1} for out-of-phase movement of the Al adsorbate and the Al_4

against the O_2 atoms. It should be emphasized that these assignments of the frequencies are approximate, as the vibrational motion of the adsorbate is highly coupled with that of the surface because of the same masses. Furthermore, test calculations with a larger cutoff radius of 4 Å (used to identify atomic degrees of freedom used in the Hessian construction) have shown that while the characters of the eigenmodes, which mainly involve adsorbate motion, remains the same, the absolute values of the frequencies can change but those changes are typically less than 50 cm^{-1}.

It can be seen from Table 5 and 6 that the Al is coordinated to the three surrounding O_2 ions in a slightly asymmetric fashion. The bond distances are 1.94−2.01 Å and thus larger than the Al−O distance of 1.84 Å in bulk alumina. This can be understood in view of the electronic state of the Al adsorbate. Upon adsorption, there is significant electron transfer from the Al adsorbate to two of the three closest Al_1 atoms (see Table 7). Furthermore, the LDOS (Figure 2) shows that upon adsorption, the s-states and the p-states of the Al atom hybridize and that two of the three peaks are still present at an energy of -1.5 eV when the Al is adsorbed, but the p-state at the Fermi level for gas-phase Al atom is only present as a very small peak at an energy of -0.5 eV. This suggests that the oxidation state of the Al adsorbate may be viewed roughly as Al^{1+}. Regarding the binding mechanism, one can see from the charge density difference plots in Table 7 that very little electron transfer occurs in the region between the Al adsorbate and the three O_2 atoms. Likewise, in the LDOS plots the O_2 atoms largely retain their LDOS shape, even though they are shifted several eV downward in energy. This suggests that there is some interaction between the Al adsorbate s- and p-states and the O_2 atoms, but that the bonding between them is mainly electrostatic in nature. The charge density that is transferred from the Al adsorbate instead goes to two of the three surrounding Al_1 atoms ($Al_1(1)$ and Al_1-(2) according to the notation in Table 5), which causes them to move up about 0.5 Å compared to the clean surface structure (the Al_1−O_2 interlayer spacing changes from 0.12 to 0.64 and 0.65 Å, respectively). This charge transfer also manifests itself in the LDOS of the $Al_1(1)$ and the $Al_1(2)$ atoms, where electronic states close to the Fermi level appear, due to interaction with the p-states of the Al adsorbate atom. As the $Al_1(1)$ and $Al_1(2)$ atoms get reduced, their bond lengths to the surrounding O_2
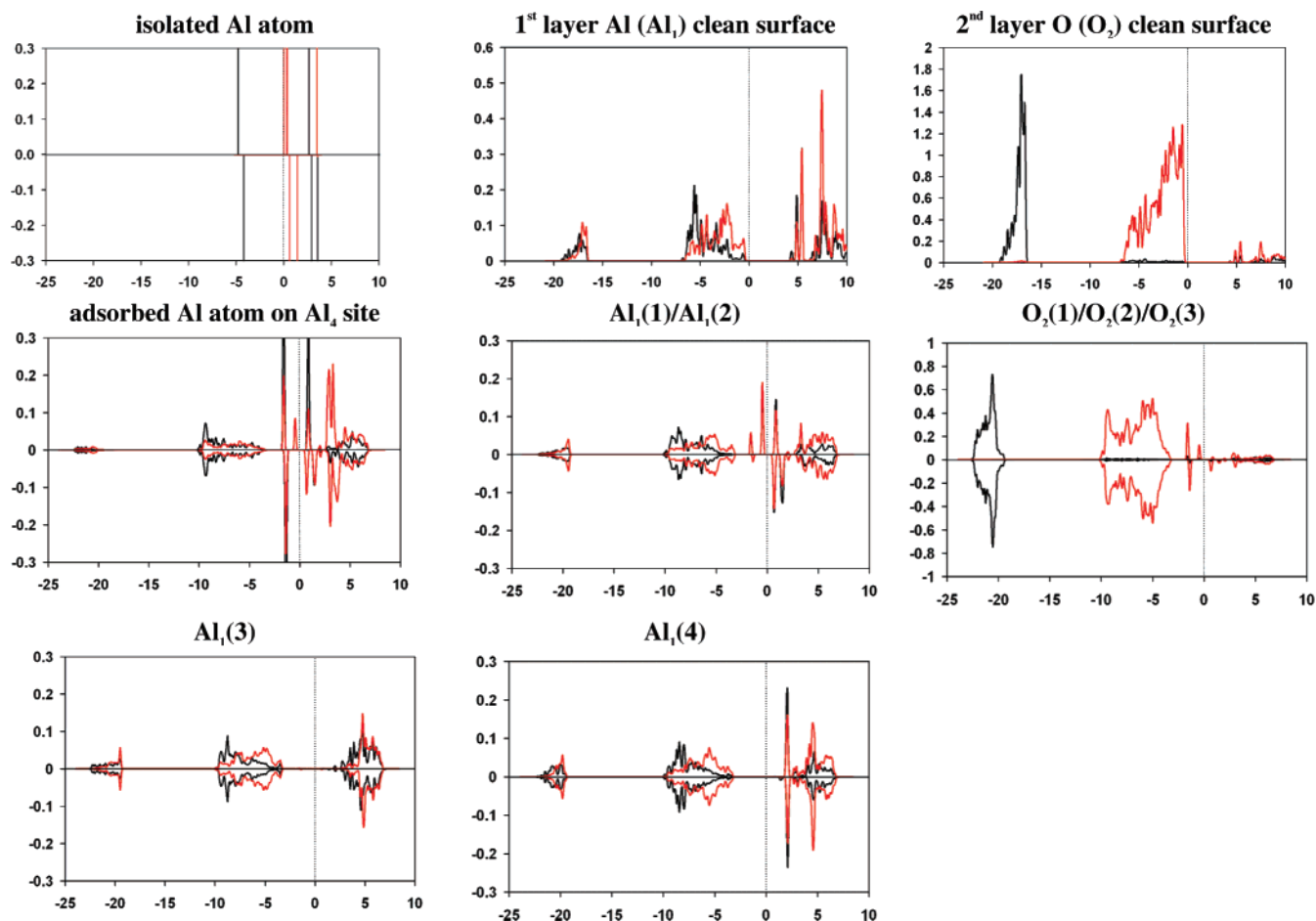
Figure 2. Site-projected angular-momentum-resolved LDOS (in number of states/unit cell) versus energy (in eV) for the isolated Al atom in the gas phase, for the Al₁ and O₂ atoms on the clean surface, and for both adsorbate and relevant surface atoms upon adsorption. The numbering of the atoms corresponds to the one in Table 5. The Fermi level is at 0 eV and is marked by a vertical line. In all plots, the color code is: black (s-states), red (p-states), and blue (d-states). For the spin-polarized calculations, negative LDOS corresponds to β-spin states, positive to α-spin states. The calculations for the clean surface have been carried out non-spinpolarized, and the LDOS is therefore twice as large as for the spin-polarized calculations. Thus, in the plots for the clean surface the LDOS scale has been made twice as large as for the spin-polarized plots so that a direct comparison is possible. The same convention is used in subsequent figures. The LDOS of Al₁(1) and Al₁(2) are practically identical; therefore, only the LDOS for Al₁(1) is shown. Likewise, the LDOS of the three O₂ atoms are practially identical, and thus only the LDOS for O₂(1) is shown.

atoms increase from 1.70 to ∼1.8 Å. This can be viewed as a process opposite to the contraction of the Al₁ atoms into the surface upon creation of the α-Al₂O₃(0001) surface. The latter process was discussed by others (e.g., Gautier-Soyer et al.[49] and Ruberto et al.[79]) who pointed out that the inward relaxation of Al₁ on the surface is due to the charge transfer from the Al₁ to the O₂ atoms, which causes a reduction of the Al−O distance of 1.87 Å in the bulk to 1.70 Å at the surface. Here, restorative charge transfer from the Al adsorbate to the two Al₁ atoms increases the bond lengths, although not all the way back to the bulk Al−O distance.

Interestingly, charge transfer and subsequent upward movement only involves Al₁(1) and Al₁(2), but not the third nearby Al₁(3) atom. Instead, Al₁(3) moves further into the bulk and its LDOS reveals no states near the Fermi level like those found for the other Al₁ atoms. Instead, its LDOS is similar to that found for Al₁(4), an Al₁ atom further away from the Al adsorbate. We have carried out test calculations on structures in which all three close Al₁ atoms were lifted, but upon structural relaxation, the original Al₄ site adsorption structure was recovered.

3.2. O on α-Al₂O₃. We find three stable sites for oxygen atom adsorption, Al₁, O₂, and O₅, for which the vibrational frequency calculations indicate that all three structures are local minima.

The most stable structure is for O adsorption on the O₂ site with an adsorption energy of −2.18 eV (same value with the dipole correction) and a magnetic moment of zero, as listed in Table 3. The vibrational frequencies that involve adsorbate motion are all greater than 200 cm⁻¹, and this allows us to unambiguously identify this site as a local minimum. The vibrational modes of the adsorbate are strongly coupled to those of the surface, and therefore separation of adsorbate modes is impossible. Therefore, in Table 4 we choose to list all vibrational frequencies that involve adsorbate motion with one component of the eigenvector >0.05 Å, and we obtain frequencies in the range 206−876 cm⁻¹.

Another local minimum is the adsorption of O on the Al₁ site with an adsorption energy of −1.75 eV (−1.74 eV including dipole correction). However, this structure is a very shallow local minimum (see Table 4) so that it is difficult to calculate accurate frequencies for the two frustrated modes parallel to the surface. By calculating the vibrational frequencies for several displacements of 0.02 to 0.05 Å, we confirm that the two small frequencies are indeed real and obtain values of ∼11 and ∼65 cm⁻¹. As for vibrational modes involving adsorbate movement perpendicular to the surface, we find two modes of ∼208 cm⁻¹ and ∼211 cm⁻¹ with in-phase motion of the O adsorbate and
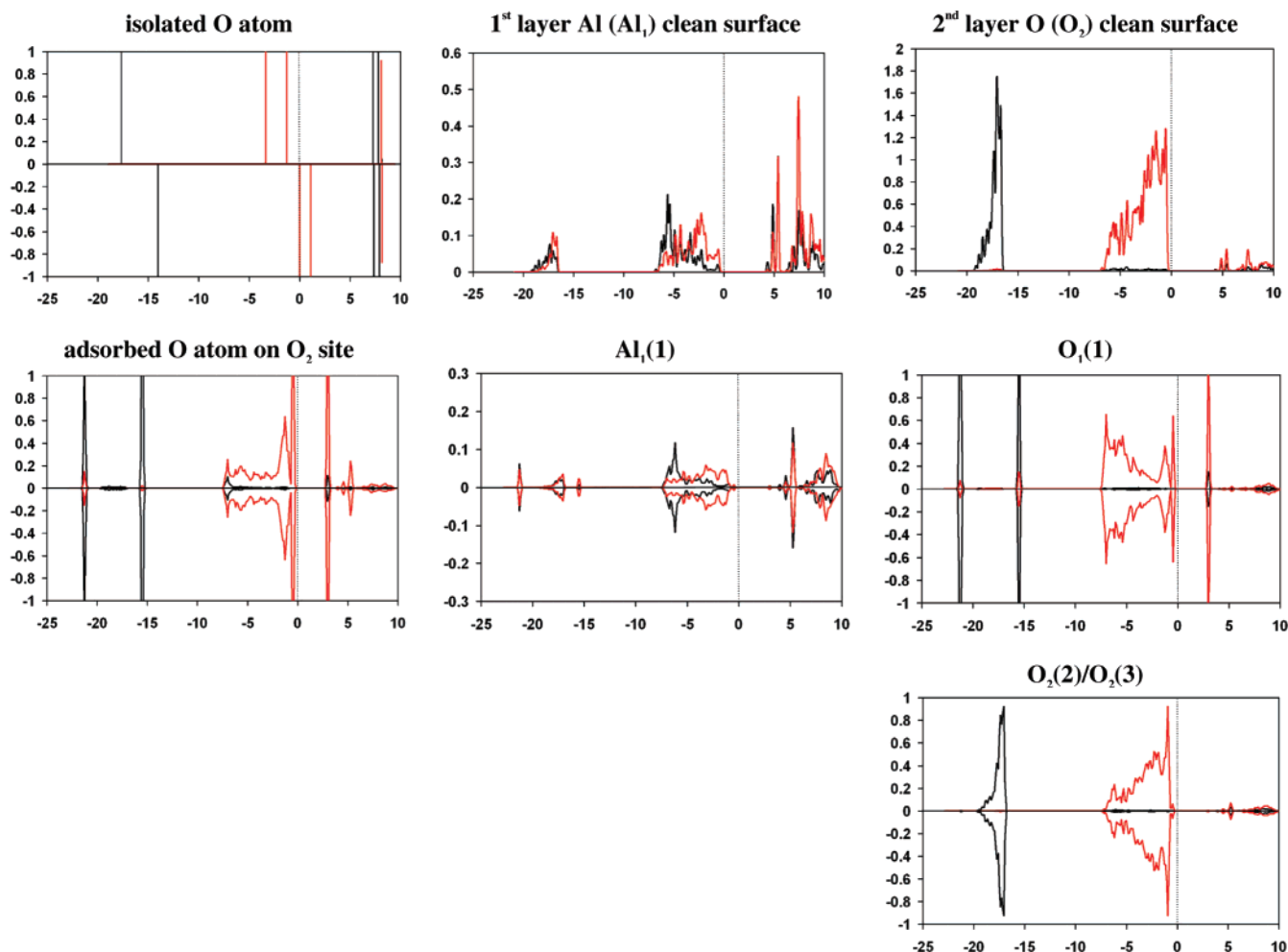
Figure 3. Site-projected angular-momentum-resolved LDOS (in number of states/unit cell) versus energy (in eV) for the isolated O atom in the gas phase, for the Al_1 and O_2 atoms on the clean surface, and for both adsorbate and relevant surface atoms upon adsorption. See the caption for Figure 2 for further explanation. The LDOS of $O_2(2)$ and $O_3(3)$ are practically identical; therefore, only the LDOS for $O_2(2)$ is shown.

underlying Al_1 atom, and a frequency of ~ 635 cm^{-1} for out-of-phase motion.

The third local minimum is adsorption of O on the O_5 site, where the O adsorbate is rather weakly bound with an adsorption energy of only -0.43 eV (same value with dipole correction). Also, for this structure it is impossible to separate adsorbate and surface motion, and the frequencies involving significant adsorbate motion are in the range 203–903 cm^{-1}, allowing for an unambiguous identification of this site as a local minimum.

We now take a closer look at the geometric and electronic structure of adsorption at O_2, as this is the most stable site. Regarding the geometry, we see in Table 5 that the O atom is not only bound to the underlying O_2 but is tilted toward the neighboring Al_1 atom, which in turn moves up by about 0.4 Å to create an interlayer spacing of 0.54 Å as compared to 0.116 Å on the clean surface (see Table 6). The distance of the O atom to the underlying oxygen atom is 1.55 Å, somewhat longer than in the O_2 (gas) molecule (1.2075 Å) and the O_2^- (gas) molecule (1.35 Å).[91] Upon binding to the O adsorbate, the Al_1 bond length to the O atom below the O adsorbate ($O_2(1)$ according to the notation in Table 5) increases by about 0.1 Å and is comparable in length to the bond length between O_{ads} and Al_1.

The charge density difference plot in Table 7 shows a significant charge transfer from the underlying O in the $O_2(1)$ site to the O adsorbate. There is no significant charge transfer

to the $Al_1(1)$ atom, but the electron density cloud is clearly tilted toward the Al_1 atom, which shows that it interacts with the O adatom.

The LDOS plots in Figure 3 suggest that a covalent bond is formed between the O adsorbate and the underlying $O_2(1)$ atom, because the LDOS of these two atoms undergo significant changes compared to the clean surface and the O atom in the gas phase. The p-states of O_{ads} and $O_2(1)$ interact and form bonding and antibonding states (as do the s-states, indicating a strong interaction between these two atoms). This suggests that a peroxo-like O_2^- or O_2^{2-}-like molecular species has formed, which is consistent with the observed electron transfer from the negatively charged $O_2(1)$ atom to the neutral O atom adsorbate, the lack of a magnetic moment, and the bond length that is longer than O_2^- (gas). This electron-rich peroxo species then tilts to establish an attractive electrostatic interaction with $Al_1(1)$, which does not appear to involve charge transfer. Even though the $Al_1(1)$ is coordinated to O_{ads}, its LDOS is only affected slightly upon adsorption, which is in line with the absence of charge transfer.

3.3. Hf on α-Al$_2$O$_3$. We find three local minima for adsorption of Hf on the surface: the Al_1, Al_3, and Al_4 sites. On the Al_1 site, Hf is located 2.9 Å above the surface and is very weakly bound with a binding energy of only -0.74 eV (-0.71 eV with dipole correction). This local minimum is very shallow with frequencies of ~ 13 and ~ 20 cm^{-1} for vibrational move-

Figure 4. Site-projected angular-momentum-resolved LDOS (in number of states/unit cell) versus energy (in eV) for the isolated Hf atom in the gas phase, for the Al₁ and O₂ atoms on the clean surface, and for both adsorbate and relevant surface atoms upon adsorption. See the caption for Figure 2 for further explanation. The LDOS of Al₁(1) and Al₁(2) are practically identical; therefore, only the LDOS for Al₁(1) is shown. Likewise, the LDOS of the three O₂ atoms are practially identical, and thus only the LDOS for O₂(1) is shown. As a semicore PAW potential is used for Hf, the 5p states are also visible at −32.3 and −31.6 eV.

ment of the Hf parallel to the surface and a frequency of ∼61 cm⁻¹ for movement perpendicular to the surface. Because the Hf atom is much heavier than the Al and O surface atom, eigenmodes of the adsorbate are only weakly coupled to those of the surface and, therefore, they can be separated easily. This weakly adsorbed state resembles adsorption of Al on Al₁, except that adsorption of Hf on Al₁ is a local minimum whereas adsorption of Al on Al₁ is a HOSP. However, because Hf is only very weakly bound in this state, we do not consider it further at present.

Hf can also adsorb on the Al₃ site and for this site we find two stable structures with two different magnetic moments: one structure in which the Hf atom loses its magnetic moment and which is a local minimum, and one metastable structure, which has a magnetic moment of 2μ_B and is a HOSP. These two

different structures have been obtained by starting the calculation with a magnetic moment of 0 or 2μ_B on the Hf atom, respectively. The local minimum structure with zero magnetic moment has an adsorption energy of −3.52 eV (same value including dipole correction) and the vibrational frequencies of the adsorbate eigenmodes are ∼88 and ∼96 cm⁻¹ for the two frustrated modes parallel to the surface and ∼136 cm⁻¹ for the mode perpendicular to the surface. The potential surface for the magnetic HOSP state is rather shallow with an imaginary frequency of 36i cm⁻¹ for movement parallel to the surface.

The most stable adsorption site and a local minimum is the Al₄ site on which we will concentrate in what follows. The adsorption energy is −4.28 eV (−4.27 eV including dipole correction) and upon adsorption, the Hf atom loses its magnetic moment. The vibrational frequencies resemble those of the
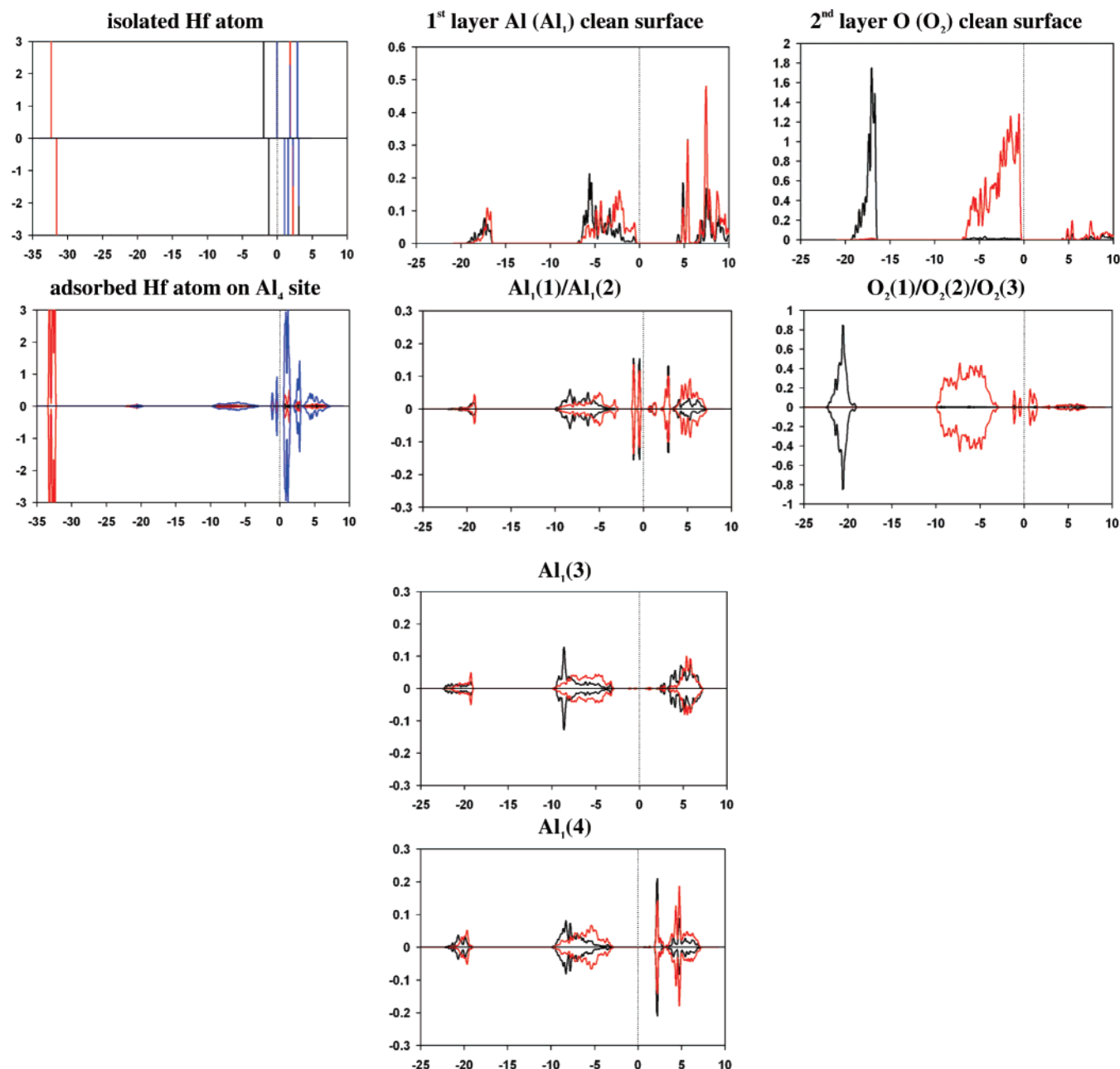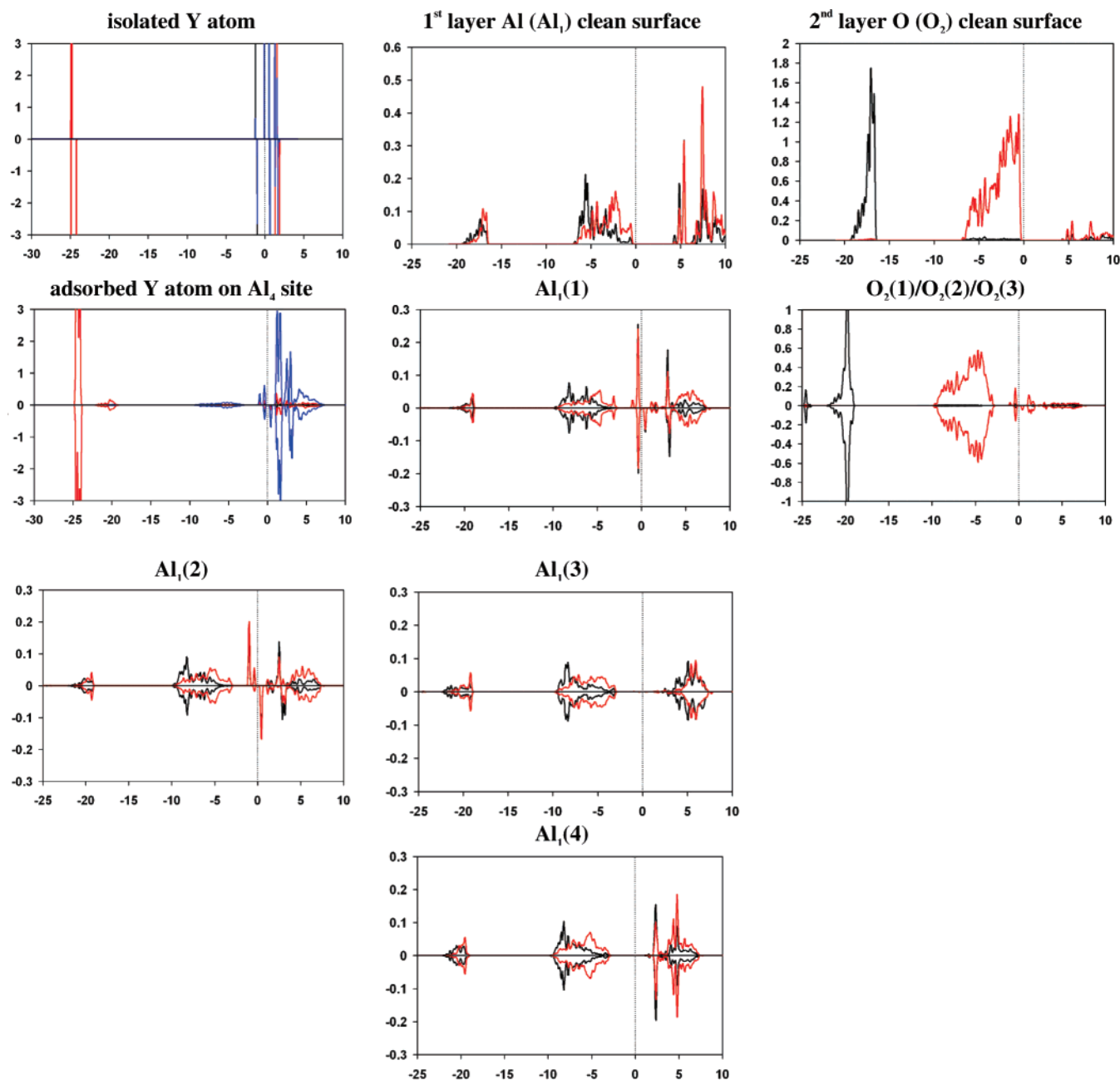
Figure 5. Site-projected angular-momentum-resolved LDOS (in number of states/unit cell) versus energy (in eV) for the isolated Y atom in the gas phase, for the Al_1 and O_2 atoms on the clean surface, and for both adsorbate and relevant surface atoms upon adsorption. See the caption for Figure 2 for further explanation. The LDOS of the three O_2 atoms are practially identical; therefore only the LDOS for $O_2(1)$ is shown. Note that for the Y atom a semicore PAW potential has been used so that the 4s and the 4p states are included in the calculation. The semicore 4p states are shown, whereas the semicore 4s states at $E-E_F \sim -45$ eV are not shown as they are unaffected by adsorption.

nonmagnetic adsorption on Al_3 and we obtain ~ 92 and ~ 105 cm^{-1} for the two frustrated modes parallel to the surface and 125 cm^{-1} for the eigenmode perpendicular to the surface.

From Table 5 and Table 6, we see that upon adsorption on the Al_4 site, the Hf atom is coordinated to the three surrounding O_2 atoms in a slightly asymmetric fashion. The reconstruction of the surface is very similar to the one caused by the adsorption of Al on the Al_4 site, except that it is significantly more pronounced. Upon adsorption, two of the three surrounding Al_1 atoms (denoted as $Al_1(1)$ and $Al_1(2)$ in Table 5) move up by about 0.8 and 0.7 Å, respectively (from an interlayer spacing of 0.12 to 0.89 and 0.79 Å, respectively). This already indicates that significant electron transfer from the Hf adsorbate to the

two Al_1 atoms is taking place. The third nearby $Al_1(3)$ atom moves deep down into the bulk to about 0.5 Å below the O_2 atoms.

From the charge density difference plot in Table 7, one can see that a significant amount of charge is transferred from the Hf atom to the two neighboring $Al_1(1)$ and $Al_1(2)$ atoms. Similar to Al adsorption, very little charge is transferred from the Hf to its closest neighbors, the three O_2 atoms, presumably because they are already nearly closed-shell (O^{2-}). One can estimate the amount of charge transfer by looking at the LDOS plots in Figure 4. The ground state atomic configuration of Hf is ^3F ($6s^2 5d^2$) and in the LDOS plot for atomic Hf in the gas phase, these four electronic states can be seen (the two d-states are
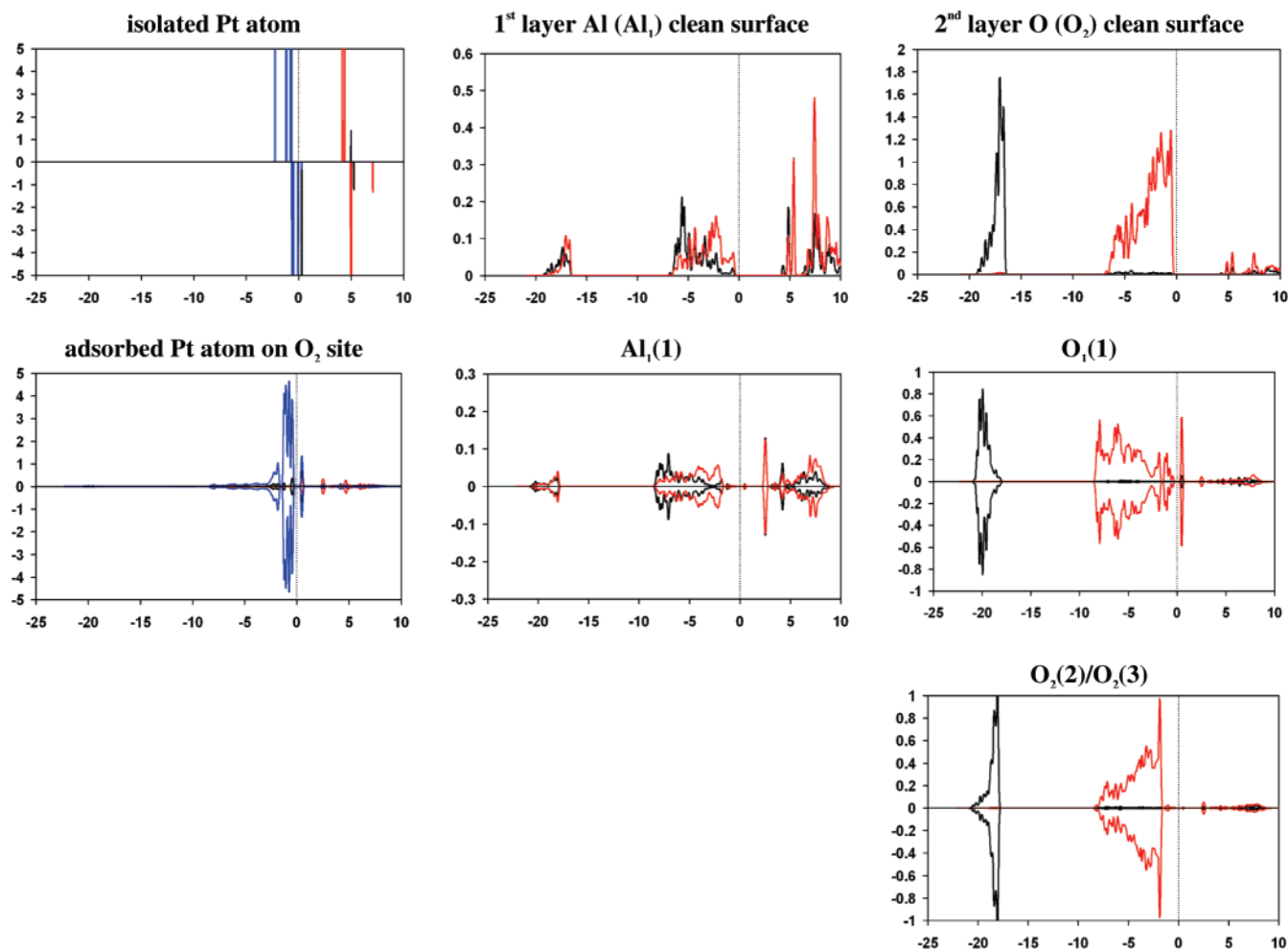
Figure 6. Site-projected angular-momentum-resolved LDOS (in number of states/unit cell) versus energy (in eV) for the isolated Pt atom in the gas phase, for the Al_1 and O_2 atoms on the clean surface, and for both adsorbate and relevant surface atoms upon adsorption. See the caption for Figure 2 for further explanation. The LDOS of $O_2(2)$ and $O_3(3)$ are practically identical; therefore, only the LDOS for $O_2(2)$ is shown.

degenerate and fall both on the Fermi level). Upon adsorption, some density of states of both s- and d-character remains below the Fermi level, but the peaks are relatively small. Therefore, we speculate that the oxidation state of the Hf is roughly +3 and that the Hf on the surface is present as an ionic species. The charge is transferred to two Al_1 atoms, which shifts the Al LDOS lower in energy. These two Al_1 atoms move up according to the reorganization already described for Al adsorption. As more charge is transferred to the two Al_1 atoms upon adsorption of Hf compared to Al, they correspondingly move up higher, about 0.7−0.8 Å compared to 0.5 Å in the Al case.

The LDOS of the three O_2 atoms coordinated to the Hf adsorbate changes shape upon adsorption and is shifted several eV downward. Because the O_2 atoms are already quite negatively charged, little charge transfer occurs from the Hf adsorbate to the O_2 atoms, as seen from the charge density difference plots of Table 7. Therefore, the Hf−O interaction is mainly electrostatic in nature.

The ionic nature of α-Al₂O₃ and the interaction of the surface with the adsorbates like Hf also manifests itself in the difference in adsorption energies between the Al_3 and Al_4 sites. As can be seen in the side view of the α-Al₂O₃(0001) surface in Figure 1, these sites appear to be rather similar with the only difference being that on the Al_4 site the underlying Al atom is further away from the surface than on the Al_3 site. But in the case of Hf, adsorption on the Al_4 site is 0.8 eV more stable than on the Al_3 site. Because the Hf adsorbate and the Al ions are both positively

charged, the Al_4 site is more stable because it minimizes electrostatic repulsions between Hf and Al cations.

As we have used a PAW potential for Hf, which includes the $(5p)^6$ semicore states, they are also visible in the LDOS plots in Figure 4 for both the isolated and the adsorbed Hf atoms. One can see that the 5p semicore states remain almost unaffected by the adsorption, which is in line with our result that the adsorption energy changes less than 0.1 eV when these states are not accounted for explicitly.

3.4. Y on α-Al₂O₃. Both Y and Hf are early transition metals with an open-shell atomic structure, and therefore we might expect that their adsorption site preferences, energies, and structures are very similar. Thus, many aspects that are similar to Hf will be discussed only briefly instead of being reiterated.

On the Al_1 site, Y only interacts very weakly with the surface with an adsorption energy of only −0.70 eV (−0.67 eV including dipole correction); this adsorption energy is very similar to the ones for Al and Hf adsorption on the Al_1 site. Similar to Al, but in contrast to Hf, the Al_1 site with adsorbed Y is a HOSP even though, again, the potential energy surface is very shallow around this site and correspondingly the vibrational frequencies listed in Table 4 are small.

The Al_3 site is a local minimum with an adsorption energy of −3.15 eV (same value including dipole correction). As with Hf, the Y-atom is much heavier than the surface atoms and the vibrational modes dominated by adsorbate motion can be easily identified. For the Al_3 site, we obtain frequencies of ∼116 and
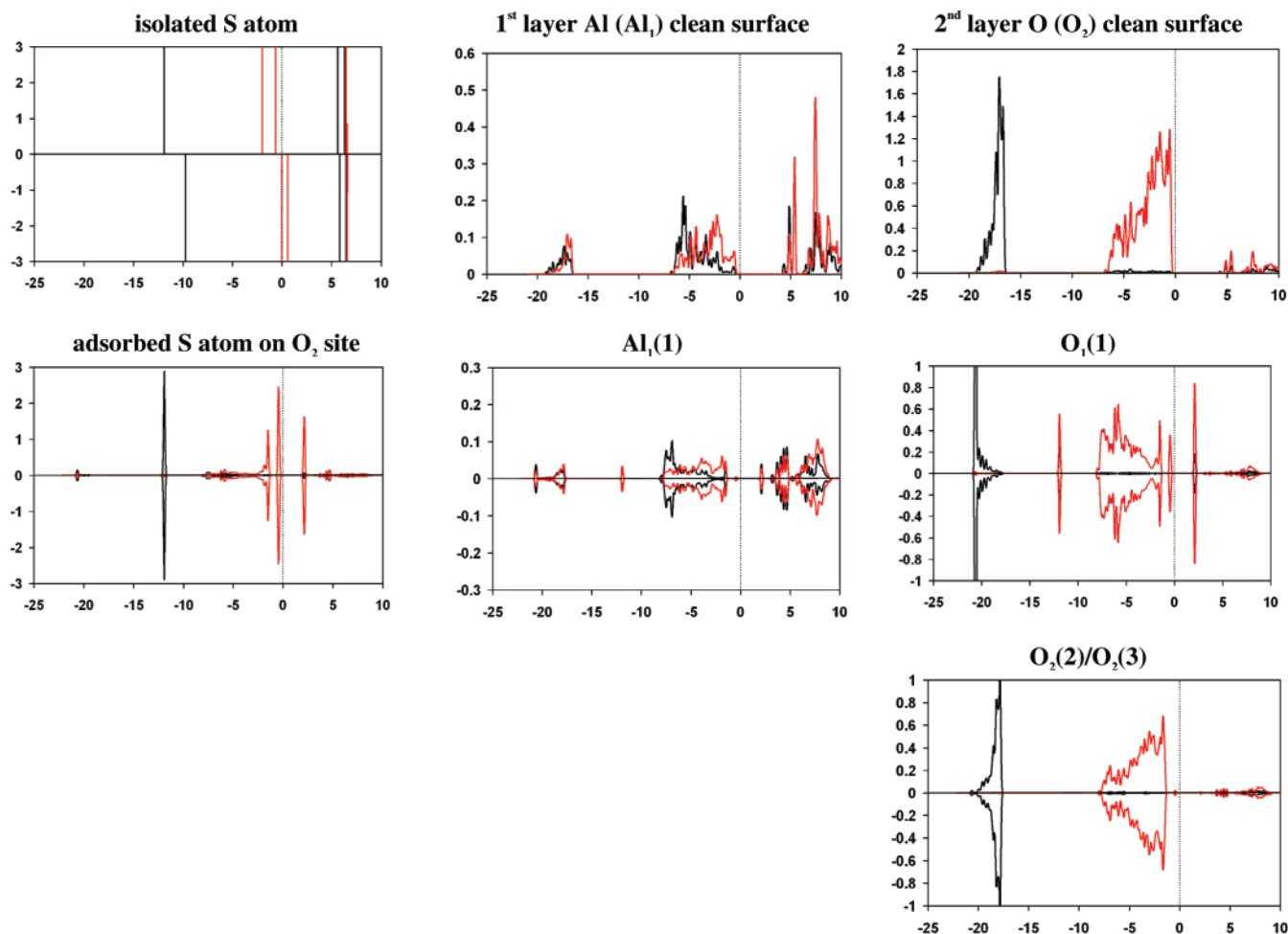
Figure 7. Site-projected angular-momentum-resolved LDOS (in number of states/unit cell) versus energy (in eV) for the isolated S atom in the gas phase, for the Al_1 and O_2 atoms on the clean surface, and for both adsorbate and relevant surface atoms upon adsorption. See the caption for Figure 2 for further explanation. The LDOS of $O_2(2)$ and $O_3(3)$ are practically identical; therefore, only the LDOS for $O_2(2)$ is shown.

$\sim$119 cm^{-1} for the two frustrated modes parallel to the surface and $\sim$174 cm^{-1} for the adsorbate mode perpendicular to the surface. Here, in contrast to Hf on Al_3 we only obtain a single structure with a magnetic moment of 1 μ_B, as there is only one unpaired electron in the system and therefore only one possible magnetic structure.

The most stable adsorption site for Y is the Al_4 site with an adsorption energy of -3.90 eV (same value including dipole correction). The vibrational frequencies are $\sim$121 and $\sim$126 cm^{-1} for the two modes parallel to the surface and $\sim$178 cm^{-1} for the mode perpendicular to the surface, similar to the ones found for the Al_3 site.

Comparing Y to Hf adsorption, one can see that the charge transfer and the resulting surface reconstructions are very similar, as seen in Tables 5 and 6 and in the charge density difference plots in Table 7. The main differences are that for Y, less electron transfer occurs than for Hf and consequently the Al_1-(1) and Al_1(2) atom, which accept the electrons transferred from the adsorbate, move up less. Furthermore, for Y adsorption the adsorbate$-O_2$ bond distances are 0.1$-$0.2 Å larger than for Hf. This can also be explained within the picture of an ionic adsorbate interacting with the surface mainly through electrostatics: as the Y adsorbate is less charged than the Hf, its bond distance to the surrounding O_2 atoms is larger (yttrium's charge requires less screening).

One can try to estimate the approximate oxidation state of Y by inspection of the LDOS plots in Figure 5. In the LDOS plot

for the Y atom in the gas phase, the 6s^2 and 5d^1 states close to the Fermi level are visible, whereas in the LDOS plot for the adsorbed Y they have been reduced to very small peaks. Therefore, one can speculate that the oxidation state of the Y-adsorbate is +2 to +3, and it is clearly present as an ionic species. The rest of the LDOS look very similar to those for Hf/Al_2O_3 and therefore we do not repeat that analysis here.

3.5. Pt on α-Al$_2$O$_3$. As Pt is a late transition metal, its adsorption characteristics on the α-Al$_2$O$_3$(0001) surface are very different from Hf and Y. The most stable site for Pt adsorption is the O_2 site with an adsorption energy of -2.02 eV. The potential energy surface around this local minimum, as with all adsorption structures for Pt, is rather shallow with frequencies of $\sim$25 and $\sim$61 cm^{-1} for the two frustrated adsorbate modes parallel to the surface and $\sim$111 cm^{-1} for the adsorbate mode perpendicular to the surface. As for all structures with small vibrational frequencies, we have calculated the frequencies using displacements of 0.02$-$0.05 Å to confirm that these frequencies indeed are real.

The other local minimum for Pt adsorption is the O_5 site with an adsorption energy of -1.60 eV (same value with dipole correction) and also with very small, but positive frequencies. The third stable adsorption site, i.e., where the Pt atom does not move spontaneously to another site during relaxation is the Al_1 site, but in this site the Pt atom is more weakly bound with an adsorption energy of -1.06 eV (same value with dipole correction). Also for this site the vibrational frequencies are very

small, but as the frequencies for the two frustrated adsorbate modes parallel to the surface are imaginary, we identify this structure as a HOSP.

In the following, we focus on the O_2 adsorption site, as this is the most stable local minimum. From Tables 5 and 6, we see that the Pt sits ontop on the O_2 atom and it is tilted slightly toward the $Al_1(1)$ atom. Similar to the adsorption of O, the Al_1-(1) atom moves up by about 0.4 Å to a height of 0.55 Å above the oxygen layer (from 0.12 Å in the bulk). This adsorption geometry resembles the one for the O atom on the O_2 site, and it is noteworthy that the adsorption energies of O and Pt are quite similar, with O binding 0.16 eV more strongly than Pt.

To analyze the binding mechanism, we turn to the charge density difference plots in Table 7 and the LDOS plots in Figure 6. In Table 7, one can see very clearly that the d_{z^2} orbital of the Pt is depleted as charge is removed from above and underneath the Pt atom. Interaction with the surface seems to take place mainly through this orbital, and it interacts with the p-electrons of the underlying $O_2(1)$ atom. Furthermore, the charge density difference plots show charge depletion on the $O_2(1)$ atom and charge accumulation close to the nearby $Al_1(1)$ atom. This charge transfer creates an unpaired electron on the $O_2(1)$ atom that enables it to form a covalent bond to the Pt adsorbate atom. This picture is confirmed by the LDOS plots. For the $O_2(1)$ atom, the p-electron LDOS clearly splits; some states are shifted downward in energy, and some form an antibonding state right above the Fermi energy. The s-electrons also are affected and shift in energy. For the Pt atom, the d-states are affected upon adsorption by broadening slightly, and they exhibit bonding/antibonding states at the same energies as the $O_2(1)$ atom, strongly suggesting formation of a covalent Pt−O bond. Little charge transfer is evident from the electron density difference plot; instead an electron redistribution about the Pt occurs to allow covalent bond formation. However, the LDOS of the isolated and adsorbed Pt atom in Figure 6 show that the singly occupied $6s^1$ state for the isolated atom (not visible because the $5d^9$ states are very close in energy on top of it in the LDOS plot) almost disappears upon adsorption. This could mean that the Pt adsorbate is positively charged but that the charge transfer is much less pronounced than for the early transition metals. It is noticeable that the electron cloud between the Pt adsorbate and $O_2(1)$ atom is shifted toward the $Al_1(1)$ atom, which explains the slight tilting in the binding geometry. The Pt−O bond length is shorter (2.03 Å) than the sum of the ionic (Shannon) radius of 1.38 Å[89] for the $O_2(1)$ atom and the covalent radius of Pt atom (1.30 Å), which is in line with the observation that the $O_2(1)$ atom loses charge upon Pt adsorption. On the other hand, the Pt−O bond length is longer than the sum of the covalent radii for O (0.66 Å) and Pt (1.30 Å), which is because the $O_2(1)$ atom is still negatively charged and thus, it is not a covalent bond of a Pt−O neutral species, but rather a negatively charged one.

3.6. S on α-Al₂O₃. S is a rather electronegative element, and therefore one would expect that it would bind favorably to a site with excess charge. Indeed, we find that the energetically most favorable adsorption site is on top the O_2 atom with an adsorption energy of −1.78 eV (same value including dipole correction). All vibrational frequencies are >120 cm⁻¹, which allows for an easy identification of the site as a local minimum, as can be seen from Table 4. As the S adsorbate is similar in atomic mass to Al and O, the adsorbate modes are strongly coupled to the surface modes, and therefore one cannot separate them. Another local minimum is the O_5 site with an adsorption

energy of −1.06 eV (−1.03 eV with dipole correction), which by vibrational analysis is readily identified as a local minimum as well.

Adsorption on the Al_1 site leads to a HOSP with an adsorption energy of −1.05 eV (−1.03 eV with dipole correction) in which the two frequencies for adsorbate motion parallel to the surface are imaginary.

Thus, S is the adsorbate that binds most weakly to the surface. As shown in Table 5, the adsorption geometry in the O_2 site resembles the one for O and Pt adsorption in which the S atom is located on top the $O_2(1)$ atom and is slightly tilted toward the nearby $Al_1(1)$ atom. The distances from S to the $O_2(1)$ and to the $Al_1(1)$ atoms (Table 6) are larger than the corresponding distances for O-adsorption. With 1.82 Å, the S−$O_2(1)$ distance is 0.27 Å larger than the O−$O_2(1)$ distance, and with 2.21 Å the S−$Al_1(1)$ distance is 0.42 Å larger than the O−$Al_1(1)$ distance. This reflects the larger size of S compared to O (covalent radius of S is 1.04 versus 0.66 Å for O), and also shows that S is not as tilted toward the nearby $Al_1(1)$ atom as O.

The electron density difference plot in Table 7 shows an accumulation of charge on top of the S atom and a depletion of charge above and below the S atom. This may be interpreted as charge transferred from the $O_2(1)$ atom to the S atom p-orbitals so as to make an S−O polar covalent bond and hence a thioperoxy anion S−O⁻ species. The $O_2(1)$ LDOS provides further evidence for this characterization in which bonding and antibonding p-states are clearly visible, which is indicative of covalent bonding. However, the LDOS of the O adatom on top of $O_2(1)$ is altered significantly more upon adsorption than is the S adatom LDOS (see Figure 7), which is in line with the weaker binding of the S atom and the larger S−$O_2(1)$ bond distance. The electron cloud is, similar to the case of O and Pt adsorption, tilted toward the $Al_1(1)$ atom, which allows for partial donation of electrons from the negatively charged SO⁻ species to the positively charged Al ion.

In general, we can conclude that S adsorption resembles O adsorption both in geometry and somewhat in electronic structure, leading to the formation of an SO⁻ species.

4. Discussion

In this section, we discuss our results and compare them to experimental and other theoretical studies where available. Furthermore, we discuss the implications of our findings on the mechanism of TBC failure.

4.1. General Trends. In general, we can divide the adsorbates into three categories: the "cationic" adsorbates Al, Hf, and Y, which preferentially adsorb on the Al_4 site and become positively charged, the "anionic" adsorbates O and S, which primarily adsorb on the O_2 site and become negatively charged, and the Pt atom, which primarily adsorbs on the O_2 site, but where only little charge transfer takes place. The cationic adsorbates Al, Hf, and Y bind to the surface primarily through electrostatic interactions, and therefore their binding energies are large. Their binding to the α-Al₂O₃ surface can be rationalized as follows: as alumina is an almost completely ionic oxide,[87,88] the O^{2-} anions have a closed-shell character that does not allow for the formation of strong covalent bonds to them (see also refs 92−93 for an in-depth discussion of these aspects). On the other hand, the early transition metals Y and Hf, and to some extent Al, can be ionized relatively easily and can therefore transfer their valence electrons to two of the electron-poor Al_1 atoms nearby. These surface Al_1 atoms readily accept electrons and then adopt a more bulklike structure commensurate with

7122 *J. Phys. Chem. C, Vol. 111, No. 19, 2007*

Hinnemann and Carter

their increased electron density. This charge transfer and the concurrent ionization of the Hf and Y (and to some extent Al) allows for a subsequent electrostatic interaction with the three surrounding O_2 ions, which is quite strong. The strength of the interaction and thus the bond energy and bond distances depend on the charge state of the adsorbate. As the adsorbed Hf has been estimated to have a charge of roughly $+3$, its binding energy is the strongest of all adsorbates (-4.3 eV) and is about 0.4 eV stronger than the binding energy of adsorbed Y, whose charge state has been estimated to be $+2$ to $+3$. The oxidation state of adsorbed Al has been estimated to be $+1$; hence, it has a significantly weaker binding energy with -2.3 eV. As discussed earlier, the upward movement of the two surrounding Al_1 atoms that get reduced can be correlated with the charge states and the binding energies, having the order Hf > Y > Al. This electron transfer from an (electropositive) adsorbate has been observed for a variety of other adsorbates that preferentially adsorb on the Al_4 site, among them Cu,[83,84,94,95] Ag,[83] and Ga.[96] For example, the Cu atom has been predicted to oxidize to Cu^{1+} upon adsorption.[95] As it is a late transition metal and therefore not as easily oxidized, its binding energy is significantly smaller, $\sim$1.1 eV.[83] However, only general upward movement of the Al_1 atoms was described, and apparently the selective upward movement of only two of the three Al_1 atoms was not observed. However, the studies of Cu adsorption were carried out at a higher coverage of 1/3 ML,[83,84] which might cause any adsorbate-induced rearrangement of the surface to be slightly different.

The adsorption mechanism for the O, S, and Pt adsorbates is different, because they are located on top of an O_2 (O^{2-}) ion in the most stable adsorption structure and form a covalent bond with this underlying atom. As already discussed, the O ion in alumina has an oxidation state of -2 and is therefore closed-shell in character. Thus, it cannot form strong covalent bonds. In the case of O, the binding mechanism is a combination of charge transfer and covalent interaction and leads to a formation of a peroxo-like O_2^- species. Adsorption of sulfur is similar, as charge transfer from O to S occurs, and S–O covalent bonding is also evident. In the case of Pt, we do not see significant charge transfer, and the covalent bond of Pt to the O_2 atom is rather weak. The adsorption of all three elements also suffers from electron pair–electron pair repulsion, and therefore the bonds are rather weak. Thus, for the bond energies we arrive at the order O > Pt > S, and the relatively weak interaction between surface and adsorbates is due to the ionic character of the α-Al_2O_3 oxide ions.

4.2. Comparison to Experimental and Other Theoretical Studies. *4.2.1. Al on α-$Al_2O_3(0001)$.* Experimental studies on adsorption and growth of Al on α-Al_2O_3 show that growth follows the Stranski–Krastanov growth mode (shown by X-ray photoelectron spectroscopy),[3] i.e., the Al atoms form one monolayer before three-dimensional growth begins. This would suggest that any coverage dependence in Al adsorption should be small; this seems probable, as the interactions of the Al adsorbates with the surface are local. Indeed, preliminary calculations in our group[97] indicate that there is a negligible coverage effect between 1/12 ML and 1/3 ML coverage.

As discussed in ref 86, even though α-Al_2O_3 is the most stable polymorph of alumina, its growth at temperatures $<$1000 °C is difficult and requires techniques like energetic bombardment, nucleation layers, or a combination of both. Proposed reasons for these difficulties are diffusion barriers high enough to hinder equilibration and that stabilize metastable phases during nucleation (see ref 86 and references therein). However, a consistent

picture has not yet emerged, and thus detailed comparison of theoretical results to experimental studies is not possible at present.

There are only few theoretical studies regarding adsorption of single Al atoms on the α-$Al_2O_3(0001)$ surface.[86,98,99] The only theoretical investigation with results that should be directly comparable to ours was published very recently by Wallin et al.[86] These researchers examined the adsorption of Al and O atoms on the α-$Al_2O_3(0001)$ surface with different terminations, among them the most stable termination with a single Al layer on which we focus here. Generally, the authors come to the same conclusion that Al preferentially binds to the Al_4 site, which also is the only local minimum, and that the interaction is predominantly ionic. However, as the size of the unit cell and the computational setup are comparable, we were puzzled that they calculated a binding energy of -3.9 eV for Al in the Al_4 site, significantly larger than our result of -2.3 eV. To find the origin of this discrepancy, it is necessary to consider in detail how the calculations were done. Wallin et al. model the α-Al_2O_3-(0001) surface with a 2×2 unit cell (as we do), and they use a slab of four stoichiometric layers (12 atomic layers) out of which they keep the bottom six atomic layers fixed in their bulk positions. By contrast, we use six stoichiometric layers and allow all the atoms to relax. As previously presented in Table 2, we have tested that this approach reproduces the adsorption energy for Al on a 9-layer slab, which as shown by Verdozzi et al.[50] creates a bulklike structure in the middle of the slab and therefore leads to accurate adsorption energies compared to an 18-layer slab. Our test calculation in which we kept four bottom atomic layers fixed (as opposed to six in Wallin et al.) leads to a significantly higher adsorption energy for Al on the Al_4 site (-5.4 eV). As already discussed earlier, this discrepancy is due to the ionicity of alumina, which causes the creation of a large dipole moment across the slab, if layers are held fixed on one side of it. Thus, we speculate that the adsorption energy of Al is sensitive to the magnitude of this artificial dipole moment, and therefore it is important to avoid this artificial dipole moment altogether. Wallin et al. also mention that the number of fixed layers may corrupt the results, and therefore it is important to carefully choose the number of fixed layers and the number of total layers. In contrast, we choose to work without fixed layers altogether, and we validate our results against a 9-layer slab, which is sufficient to provide a bulk-like environment in the middle of the slab. It should be noted, though, that in spite of these technical differences in the calculations, the conclusions of Wallin et al. largely agree with ours. Note that for surfaces with different terminations, the Al adsorption energy varies noticably, being strongest on the oxygen-teminated surface and weakest on the hydroxylated surface.

Another study of the adsorption of Al on the oxygen-terminated α-$Al_2O_3(0001)$ surface was carried out by Rosén et al.,[98,99] also considering a coverage of 1/12 ML. As they consider an oxygen-terminated surface, the results are not directly comparable. However, they also find the Al_4 site to be most stable, but they find that the Al atom adsorbs symmetrically between the O_2 atoms. In contrast, on the Al-terminated surface we find that the adsorption is asymmetric, presumably caused by the Al_1 atoms. As they considered Al ions and a negatively charged surface as a starting point, the adsorption energies cannot be compared.

As we have seen, only very limited experimental information is available regarding Al adatoms on the α-$Al_2O_3(0001)$ surface. However, because the Al/α-Al_2O_3 interface is commonly used

in electronic and structural applications, it is rather well studied, and therefore it is instructive to briefly discuss it here. The Al-(111)/α-Al$_2$O$_3$(0001) interface has been studied both experimentally[3,100−103] and theoretically.[104,105] Several experimental studies have determined the work of adhesion for this interface to be 0.41−1.13 J/m^2.[100−103] Theoretical investigations of the Al(111)/α-Al$_2$O$_3$(0001) interfaces,[104,105] which employ the same Al-terminated α-Al$_2$O$_3$(0001) surface as we consider, find that in the most favorable interface structure the Al atoms of the Al-(111) surface are located in the Al$_1$, Al$_3$, and Al$_4$ adsorption sites (designated "atop Al" by Smith et al.[104] and "fcc" by Siegel et al.[105]). We can understand this result by noting that the Al$_4$ site is the most favorable adsorption site and is presumably the one that is responsible for most of the adhesion. This assumption is corroborated by the observation of Siegel et al.[105] that the Al atom bound to the Al$_4$ site is somewhat removed from the Al-(111) layer and drawn closely to the α-Al$_2$O$_3$(0001) surface, where it binds to the Al$_4$ site and gives rise to similar reconstructions as observed in the present study. The adhesion energy for this interface structure is determined by Smith et al.[104] as 1.078 J/m^2 and by Siegel et al.[105] as 1.06 J/m^2. For this interface, an adhesion energy of 1 J/m^2 corresponds to a bond energy of ∼ −0.4 eV per bond. This value is much smaller than the bond energy for an isolated Al atom, which shows that the overall bonding mechanism is very different for Al within the metallic surface. The two situations can only be compared to a limited extent, as the isolated Al atom binding clearly involves localized charge-transfer that cannot readily occur in the metallic overlayer case.

4.2.2. O on α-Al$_2$O$_3$(0001). In contrast to Al adsorption, three local minima for O adsorption have been found, and the two minima with the lowest adsorption energy agree with the ones found by Wallin et al.[86] Comparing the adsorption energies of O on O$_2$ (our result, −2.18 eV; Wallin et al., −2.3 eV) and on Al$_1$ (our result, −1.75 eV; Wallin et al., −1.8 eV), one can see that they agree quite well, despite the differences in surface thickness and constraints, as discussed in the previous section. We speculate that as the interaction of O with the surface is mainly covalent and causes no major reconstruction, it is influenced much less by a possible artificial dipole of the slab. In contrast to Wallin et al., we also find adsorption on the O$_5$ site to be a local minimum, albeit with a much weaker binding.

In previous studies of α-Al$_2$O$_3$ thin film growth,[86,98,99] it was discussed that formation of thermodynamically less stable transient phases might be caused by kinetic trapping due to high barriers to diffusion of the deposited oxygen species. This would be in line with our findings regarding both the nature of the O adsorbate (bound as a peroxy species) and the presence of several stable adsorption sites. A high barrier to O diffusion may be anticipated because of the need to break a covalent O−O bond to diffuse to a new site. Additionally, the O diffusion pathways may visit these higher energy adsorption sites, which would also raise the effective overall barrier to O diffusion. This will be the subject of a forthcoming study.[32]

4.2.3. Hf and Y on α-Al$_2$O$_3$(0001). To our knowledge, no experimental or theoretical investigations probing the interaction of Y and Hf with α-Al$_2$O$_3$(0001) have been performed, so no direct comparison of our results is possible. However, it is well known that in bulk α-Al$_2$O$_3$ the dopants Hf and Y substitute for the Al^{3+} ion. Y is a common dopant in α-Al$_2$O$_3$ and improves its thermomechanical properties (e.g., by limiting creep) considerably by segregating to GBs and hindering their motion.[17−22] In this context, we can rationalize our findings that both Hf and Y preferentially bind on the Al$_4$ site, the same site

as for Al adsorption, and also the site where Al or cationic dopants would adsorb to continue the corundum bulk structure. One theoretical study[106] did calculate the adsorption of Y on a thin film of Al$_2$O$_3$ on Al(111). At 1/3 ML coverage, Y is predicted to adsorb preferentially in the threefold hollow site that has no Al ion underneath with an (local density approximation, or LDA) adsorption energy of −6.9 eV. This binding energy is considerably stronger than what we find for Y on the Al$_4$ site (−3.9 eV). This is in part due to the usual LDA overbinding, but is likely also due to the very real possibility that an adsite lacking a positively charged Al ion nearby may lead to a larger binding energy. Considering these two factors, our results are roughly consistent with those of Bogicevic et al.[106]

We also note that Y and Hf bind strongly to the alumina surface, because they are ionized and can interact electrostatically with the underlying negatively charged O$_2$ atoms. In this context, it is interesting to consider briefly the properties of the bulk oxides Y$_2$O$_3$ and HfO$_2$. Both HfO$_2$ and Y$_2$O$_3$ are refractory oxides and insulators[107,108] with HfO$_2$ being a wide band gap material that may have the potential for substituting SiO$_2$ as gate electronics in microelectronic devices.[109] Both HfO$_2$ and Y$_2$O$_3$ are of predominantly ionic character with Y$_2$O$_3$ being slightly less ionic than α-Al$_2$O$_3$.[107] These properties are consistent with our findings that Hf and Y replace Al in the cation position and hence should adsorb preferentially on the same site and through the same bonding mechanism.

4.2.4. Pt on α-Al$_2$O$_3$(0001). As Pt/Al$_2$O$_3$ is of fundamental importance in catalysis, numerous experimental and theoretical studies have been carried out.

In general, previous theoretical studies agree on the binding site and energy, but present different views with regard to the bonding mechanism. Verdozzi et al.[50] studied Pt adsorption on α-Al$_2$O$_3$(0001) at coverages of 1 ML and 1/3 ML, and while the 1 ML Pt overlayer only binds weakly to the surface, at 1/3 ML they find a binding energy of −2.9 eV with LDA and of −2.0 eV with GGA. Their GGA result is the same as our (GGA) binding energy of 1/12 ML Pt (−2.0 eV), which shows that at low coverages there are no lateral adsorbate−adsorbate effects. In this and in a later study, they state that the bonding mechanism is predominantly ionic and thus driven by charge transfer from the Pt 6s orbital to the underlying oxygen ion.[50,106] In contrast, we find that the bonding mechanism involves charge rearrangement on Pt and covalent Pt−O bonding. Another series of theoretical studies using linear combination of Gaussian-type orbitals fitting DFT (LCGTO-FF−DF) with the BP86 GGA exchange-correlation functional[110,111] considered Pt atoms adsorbed on small alumina clusters embedded in an array of point charges. They also find that the Pt atom preferentially binds on the O$_2$ site with a binding energy of −1.7 eV. The weaker binding may be due to the finite nature of the cluster model, which cannot account completely for all structural and electronic relaxation effects. Rivanenkov et al.[110] find only the O$_2$ site to be a local minimum, whereas we also find a local minimum on O$_5$. However, characterization of metastable states is difficult because of the small frequencies associated with adsorbate motion. Moreover, characterization of the O$_5$ site may require the presence of several layers that are allowed to relax; this is only possible to a limited extent in a cluster study. Interestingly, Rivanenkov et al.[110] do not find significant charge transfer from the Pt atom to the surface, which points to a more covalent bonding mechanism. This is in line with our findings, which do not show a significant charge transfer from the Pt to the surface O$_2$ atom.

In this context, we briefly mention that Pd adsorbs on α-Al$_2$O$_3$(0001) in quite a similar way to Pt, and the former

system has been studied much more thoroughly, both experimentally by deposition of Pd clusters on thin alumina films (ref 34 and references therein) and theoretically.[50,106,110–114] In general, there is agreement that Pd preferentially binds on the O_2 site and that it binds markedly weaker than Pt. The binding mechanism is somewhat controversial. Some studies[50,106] suggest an ionic bond, whereas others[110–114] suggest that binding primarily occurs by polarization of the metal atoms in the electric field of the support with only small covalent and ionic contributions. In a recent study, Gomes et al.[115] elucidated the nature of the chemical bond of Pd on different oxide surfaces by analyzing the topology of the charge density, and for binding of Pd on the α-$Al_2O_3(0001)$ surface they found that the Pd atom remained largely neutral with only very little charge transfer to the surface. This is consistent with the closed-shell d^{10} ground state of the Pd atom, while the open-shell s^1d^9 ground state of the Pt atom lends itself to covalent bonding.

4.2.5. S on α-$Al_2O_3(0001)$. To our knowledge, no experimental or theoretical work has been reported that directly probes adsorption of S atoms on α-$Al_2O_3(0001)$. S interactions with Al_2O_3 is relevant to hydrodesulfurization catalysis in which sulfur is removed from crude oil, typically by means of an MoS_2-based catalyst on a porous γ-alumina support.[116] In this context, adsorption and dissociation of H_2S on γ-Al_2O_3 surfaces of different orientations have been studied,[117] and it is generally observed that upon dissociation, the SH group binds to a surface oxygen atom. This seems to be in line with our results, but as the structure and properties of γ-alumina are very different from α-alumina, one has to be cautious with these comparisons.

4.3. Implications for Thermal Barrier Coatings. Having placed our results for adsorption of Al, O, Hf, Y, Pt, and S on α-Al_2O_3 in context by comparing and validating against previous experimental and theoretical work, we now turn to the consequences of our findings for the mechanisms of TBC failure. We focus on adhesion of the TGO to the underlying (Pt)NiAl bond coat and on failure due to the growth of the TGO.

Several experimental studies[10,25] have shown that S is detrimental to TBC interface adhesion and causes rapid spallation of the TGO. In contrast, Pt has been observed to be beneficial to TBC stability, and as it does not influence the TGO growth kinetics, it has been suggested that its role might be to improve adhesion. To discuss the implications of our results for TGO/bond coat adhesion, we compare them to two previous studies from our research group in which the adsorption of Hf, Pt, and S on NiAl(110)[118] and the influence of these elements on the adhesion of the NiAl(110)/α-$Al_2O_3(0001)$ interface[119] were investigated. First, all dopant and impurity elements bind more strongly to the NiAl(110) surface than to the α-Al_2O_3-(0001) surface. Furthermore, the adsorbate binding energies to the NiAl(110) surface are rather similar: -5.0 eV for Hf, -5.3 eV for Pt, and -4.9 eV for S on their respective minimum energy sites.[118] In contrast, we find that the adsorption energies of Hf, Pt, and S on the α-$Al_2O_3(0001)$ surface vary drastically; whereas Hf is strongly bound (-4.3 eV), Pt and S are bound much more weakly (-2.0 and -1.8 eV, respectively). This means that adhesion of the NiAl(110)/α-$Al_2O_3(0001)$ interface upon dopant or impurity segregation is clearly determined by how well the dopants bind to the α-$Al_2O_3(0001)$ surface. Indeed, it is found that adhesion of the interface is significantly strengthened by Hf (2.06 J/m^2 compared to 0.66 J/m^2 without dopants), significantly weakened by S (0.18 J/m^2), and slightly weakened by Pt (0.53 J/m^2).[119] Combining these results with the present study, we can conclude that Hf improves adhesion, because it binds strongly to the α-$Al_2O_3(0001)$ surface due to

an ionic bond created by ionization of the Hf and charge transfer to the α-$Al_2O_3(0001)$ surface. As Pt only binds weakly to the α-$Al_2O_3(0001)$ surface, it cannot improve interface adhesion, and as S binds even more weakly than Pt it actually worsens interface adhesion. This picture explains the role of S, which weakens interface adhesion, and it elucidates one of the benefits of Hf (the other one will be discussed below), which strengthens interface adhesion by open-shell effects (similarly discussed in refs 92–93). However, the role of Pt is not yet clear, as it does not improve adhesion but rather leaves it unaltered. Its influence may be of a very different nature, as it has been observed that Pt hinders spinel formation even at high Ni contents in NiAl alloys,[120] and thus Pt may influence Ni and/or Al diffusion. Investigations of this effect are beyond the scope of the present study and will be presented elsewhere.[121] However, another interesting observation emerges from our results: on the α-$Al_2O_3(0001)$ surface, Pt binds on the same O_2 site as S but 0.2 eV more strongly and therefore may be able to displace S from this site. This suggests that the role of Pt perhaps is not to increase adhesion directly by itself, but to block sulfur from segregating to the surface site where S can weaken adhesion. This role of Pt has been suggested previously,[10] but here we present evidence that such a role of Pt is thermodynamically feasible.

Another important aspect of TBC failure is the growth of the TGO, α-Al_2O_3, that inevitably causes spallation when the TGO layer becomes too thick. Dopants like Hf, Y, and Zr have been shown to slow down TGO growth, whereas Pt does not have any effect on TGO growth. The results of the present study allow us to rationalize some of these observations. Hf and Y bind preferentially to the same Al_4 site as Al, but about 2 eV (Hf) or 1.6 eV (Y) more strongly, and can therefore act as an Al site blocker. By contrast, Pt binds to a different site and 0.3 eV more weakly than Al, and therefore it seems plausible that it should not influence Al adsorption. Hf, Y, and Zr dopants have been shown to slow down TGO growth by inhibiting Al diffusion. Our results are in line with this observation because if Hf and Y act as site blockers for Al this probably in turn limits Al diffusion. It has been proposed that dopant cations may enhance the binding of Al ions to their oxygen neighbors, thereby hindering Al diffusion.[21,22,23] Our findings suggest the opposite, namely, that Y or Hf adsorption appears to weaken rather than strengthen the nearby Al–O bonds because the Al ions are reduced and the Al–O bond lengths increase. However, definitive conclusions will require explicit consideration of this issue at an actual GB.

Because we find that O preferentially binds on a different site than Hf and Y, the effect of Hf and Y on O adsorption is likely to be less significant than for Al adsorption. Calculations of Hf or Y coadsorption with O would be needed to clarify this issue. While experiments have shown that Y and Hf inhibit cation diffusion in TGO growth,[12,18] we are unaware of any studies that directly investigate the effect of Y and Hf on oxygen diffusion. Last, even though Pt binds on the same site as O it binds 0.2 eV more weakly and therefore is not favored thermodynamically to act as a site blocker for O. Thus, Pt cannot act as a site blocker for any relevant species. Of course, one has to be aware that a GB in α-Al_2O_3 is structurally very different from the α-$Al_2O_3(0001)$ surface, but as we base our conclusions on large energy differences and very general trends we expect them to be robust.

Another interesting aspect is the question of whether neutral or ionic species diffuse through the TGO alumina layer, and in the latter case how the initially neutral species entering from

the NiAl or from the YSZ layer become ionized. Our calculations suggest that, for example, Al, Hf, and Y become partly ionized upon adsorption on the alumina surface, and the excess charge is distributed among nearby Al cations. In a similar way, O becomes negatively charged via charge donation from the O anion. Thus, upon entry into the α-Al₂O₃, it is plausible that the diffusing species become charged, which is in line with the observation that growth of the TGO is affected by an electric field, which in turn suggests that the diffusing species are charged.[13] However, we find that the Al and O adsorbate atoms are less charged than the Al and O ions in the oxide, which can be regarded as Al^{3+} and O^{2-}. This may make it easier for these ions to diffuse through the TGO because they will experience less electrostatic repulsion. The finding that Al and O adatoms on the α-Al₂O₃(0001) are partly ionized also may have implications for the charge states of species diffusing along GBs during alumina creep. In TBC growth, the metal substrate can accommodate a net charge transfer, whereas in alumina creep net charge transfer is less plausible (because creep involves mostly structural rearrangements, for example, grain-boundary sliding). Creep diffusion therefore may occur by fully ionized species. However, further elucidation of this question requires investigation of Al and O diffusion along a model GB. Such studies are in progress in our laboratory.

5. Conclusions

In this paper, we have investigated adsorption of Al, O, Hf, Y, Pt, and S on the α-Al₂O₃(0001) surface. We find that Al, Hf, and Y preferentially adsorb on the Al₄ hollow site and form strong ionic bonds to oxygen by transferring charge to the surface and themselves becoming ionized. In contrast, Pt and S preferentially adsorb on the O₂ on-top site and bind to the surface relatively weakly. For Pt, we do not observe significant charge transfer and the bond occurs mainly through adsorbate polarization and covalent bonding. For O and S adsorption, we observe electron transfer from the surface oxygen ion to the adsorbate, concomitant with covalent bond formation to form (thio)peroxy anions. These results are in line with other experimental and theoretical studies, and we have used them to rationalize a number of experimental observations regarding failure of thermal barrier coatings. Together with the results from previous studies in our group, which find strong binding of Hf, Pt, and S to NiAl(110)[118] and strengthening of the NiAl-(110)/α-Al₂O₃(0001) interface adhesion by Hf, weakening by S, and no influence by Pt,[119] we can conclude the following:

• The determining factor in the effect of segregating elements on the NiAl-based bond coat alloy/TGO (alumina) interface adhesion is how strongly bound the dopants are to α-Al₂O₃.

• Hence, Hf strengthens interface adhesion, because is binds strongly to the α-Al₂O₃(0001) surface.

• S weakens interface adhesion, because it binds weakly to the α-Al₂O₃(0001) surface.

• One possible role of Pt might be not to strengthen interface adhesion itself, but to block S from adsorbing on the α-Al₂O₃-(0001) surface and thereby to prevent it from weakening interface adhesion.

Regarding TGO growth, we have analyzed the adsorption of Al, O, Hf, and Y on the α-Al₂O₃(0001) surface and find that Al, Hf, and Y preferentially adsorb on the Al₄ site. Hf and Y bind significantly stronger than Al and therefore can act as site blockers and displace Al. O adsorbs on a different site (the O₂ site), and therefore Hf and Y cannot act as site blockers for O diffusion. From this, we can conclude the following:

• In line with experimental observations, Hf and Y might hinder Al diffusion, because they can act as a site blocker for the Al₄ site, the only site where Al adsorbs.

• Neutral Al, Hf, and Y become positively charged and neutral O becomes negatively charged upon adsorption on α-Al₂O₃-(0001), which is consistent with the observation that TGO growth occurs via charged diffusing species.

• As O adsorbs on a different site, its adsorption (and presumably its diffusion) is not significantly hindered by Hf and Y, which explains why these dopants only slow down TGO growth (by hindering Al adsorption and consequently diffusion) but do not stop it completely.

• Pt adsorbs on the same site as O but binds more weakly, which explains why it cannot act as a site blocker at all and thus does not influence TGO growth.

• Preliminary calculations with Zr (not discussed here) indicate that its chemistry on the α-Al₂O₃(0001) surface is very similar to Hf and Y, which is in line with the experimental observation that Hf, Y, and Zr dopants slow down TGO growth.

Thus, consideration of the simple case of adsorption on the α-Al₂O₃(0001) surface of various dopants and impurities present in TBCs has allowed us to rationalize several aspects of TGO growth. Of course, our model is very simple and very different from an actual TBC, but it does provide a set of baseline values and general trends. To complete the picture, we need to investigate diffusion of the adsorbed species on the surface; these results will be presented in a forthcoming study.[32] Then, when we move from this simple surface−adsorbate system to investigate the more complex case of alumina GBs, we can use the results of this study as a guideline to see how the grain-boundary structure affects our understanding of TBC failure.

References and Notes

(1) Henrich, V. E.; Cox, P. A. *The Surface Science of Metal Oxides*; Cambridge University Press: New York, 1994.

(2) Gates, B. C. *Chem. Rev.* **1995**, *95*, 511.

(3) Campbell, C. T. *Surf. Sci. Rep.* **1997**, *27*, 1.

(4) Street, S. C.; Xu, C.; Goodman, D. W. *Annu. Rev. Phys. Chem.* **1997**, *48*, 43.

(5) Padture, N. P.; Gell, M.; Jordan, E. H. *Science* **2002**, *296*, 280.

(6) Goward, G. W. *Surf. Coat. Technol.* **1998**, *108−109*, 73.

(7) Levi, C. G. *Curr. Opin. Solid State Mater. Sci.* **2004**, *8*, 77.

(8) Brady, M. P.; Pint, B. A.; Tortorelli, P. F.; Wright, I. G.; Hanrahan R. J., Jr. High-Temperature Oxidation and Corrosion of Intermetallics. In *Corrosion and Environmental Degradation*; Schütze, M., Ed.; Wiley-VCH: Weinheim, Germany, 2000; Vol. II, Chapter 6.

(9) Clarke, D. R.; Levi, C. G. *Annu. Rev. Mater. Res.* **2003**, *33*, 383.

(10) Evans, A. G.; Mumm, D. R.; Hutchinson, J. W.; Meier, G. H.; Pettit, F. S. *Progr. Mater. Sci.* **2001**, *46*, 505.

(11) Wright, I. G.; Pint, B. A. *Proc. Inst. Mech. Eng., Part A* **2005**, *219*, 101.

(12) Pint, B. A. *Oxid. Met.* **1996**, *45*, 1.

(13) Ramanarayanan, T. A.; Raghavan, M.; Petkovic-Luton, R. Al₂O₃ scales on ODS alloys. In *Proceedings of the Japan Institute of Metals International Symposium High Temperature Corrosion Transactions Supplement*; Japan Institute of Metals: Tokyo, Japan, 1983; Vol. 24 p 199−206.

(14) Quadakkers, W. J.; Elschner, A.; Speier, W.; Nickel, H. *Appl. Surf. Sci.* **1991**, *52*, 271.

(15) Hou, P. Y. *J. Am. Ceram. Soc.* **2003**, *86*, 660.

(16) Nychka, J. A.; Clarke, D. R. *Oxid. Met.* **2005**, *63*, 325.

(17) Ruano, O. A.; Wadsworth, J.; Sherby, O. D. *Acta Mater.* **2003**, *51*, 3617.

(18) Wang, C. M.; Cargill, G. S., III; Chan, H. M.; Harmer, M. P. *Acta Mater* **2000**, *48*, 2579.

(19) Gülgun, M. A.; Putlayev, V.; Rühle, M. *J. Am. Ceram. Soc.* **1999**, *82*, 1849.

(20) Fabris, S.; Elsässer, C. *Acta Mater.* **2003**, *51*, 71.

(21) Buban, J. P.; Matsunaga, K.; Chen, J.; Shibata, N.; Ching, W. Y.; Yamamoto, T.; Ikuhara, Y. *Science* **2006**, *311*, 212.

(22) Amutha, Rani, D.; Yoshizawa, Y.; Hirao, K.; Yamauchi, Y. *J. Am. Ceram. Soc.* **2004**, *87*, 289.

(23) Wang, C. M.; Cargill, S. G., III; Chan, H. M.; Harmer, M. P. *J. Am. Ceram. Soc.* **2002**, *85*, 2492.

(24) Haynes, J. A.; Pint, B. A.; More, K. L.; Zhang, Y.; Wright, I. G. *Oxid. Met.* **2002**, *58*, 513.

(25) Zhang, Y.; Lee, W. Y.; Haynes, J. A.; Wright, I. G.; Pint, B. A.; Cooley, K. M.; Liaw, P. K. *Metall. Mater. Trans.* **1999**, *30A*, 2679.

(26) Oishi, Y.; Kingery, W. D. *J. Chem. Phys.* **1960**, *33*, 480.

(27) Paladino, A. E.; Kingery, W. D. *J. Am. Ceram. Soc.* **1962**, *37*, 957.

(28) Marinopoulos, A. G.; Elsässer, C. *Acta Mater.* **2000**, *48*, 4375.

(29) Elsässer, C.; Elsässer, T. *J. Am. Ceram. Soc.* **2005**, *88*, 1.

(30) Gemming, T.; Nufer, S.; Kurtz, W.; Rühle, M. *J. Am. Ceram. Soc.* **2003**, *86*, 581.

(31) Nishimura, H.; K. Matsunaga, T. Saito, T. Yamamoto, Y. Ikuhara, *J. Am. Ceram. Soc.* **2003**, *86*, 574.

(32) Hinnemann, B.; Carter, E. A. To be submitted for publication.

(33) Freund, H.-J.; Kuhlenbeck, H.; Libuda, J.; Rupprechter, G.; Bäumer, M.; Hamann, H. *Top. Catal.* **2001**, *15*, 201.

(34) Freund, H.-J. *Surf. Sci.* **2002**, *500*, 271.

(35) Kresse, G.; Schmid, M.; Napetschnig, E.; Shishkin, M.; Köhler, L.; Varga, P. *Science* **2005**, *308*, 1440.

(36) Ahn, J.; Rabalais, J. W. *Surf. Sci.* **1997**, *388*, 121.

(37) Toofan, J.; Watson, P. R. *Surf. Sci.* **1998**, *401*, 162.

(38) Renaud, G. *Surf. Sci. Rep.* **1998**, *23*, 1.

(39) Guenard, P.; Renaud, G.; Barbier, A.; Gautier-Soyer, M. *Mater. Res. Soc. Symp. Proc.* **1996**, *437*, 15.

(40) Tasker, P. W. *J. Phys. C: Solid State Phys.* **1979**, *12*, 4977.

(41) Ciraci, S.; Batra, I. P. *Phys. Rev. B* **1983**, *28*, 982.

(42) Causà, M.; Dovesi, R.; Pisani, C.; Roetti, C. *Surf. Sci.* **1989**, *215*, 259.

(43) Mackrodt, W. C.; Thomas, J. M.; Ackland, G. *Philos. Trans. R. Soc. London, Ser. A* **1992**, *341*, 301.

(44) Guo, J.; Ellis, D. E.; Lam, D. J. *Phys. Rev. B* **1992**, *45*, 13647.

(45) Blonski, S.; Garofalini, S. H. *Surf. Sci.* **1993**, *295*, 263.

(46) Manassidis, I.; Devita, A.; Gillan, M. J. *Surf. Sci. Lett.* **1993**, *285*, L517.

(47) Manassidis, I.; Gillan, M. J. *J. Am. Ceram. Soc.* **1994**, *77*, 335.

(48) Godin, T. J.; LaFemina, J. P. *Phys. Rev. B* **1994**, *49*, 7691.

(49) Gautier-Soyer, M.; Jollet, F.; Noguera, C. *Surf. Sci.* **1996**, *352–354*, 755.

(50) Verdozzi, C.; Jennison, D. R.; Schultz, P. A.; Sears, M. P. *Phys. Rev. Lett.* **1999**, *82*, 799.

(51) Ruberto, C. Ph.D. Thesis, Chalmers University, Göteborg, Sweden, 2001.

(52) Grönbeck, H. *Top. Catal.* **2004**, *28*, 59.

(53) Lagerlöf, K. P. D.; Heuer, A. H.; Castaing, J.; Rivière, J. P.; Mitchell, T. E. *J. Am. Ceram. Soc.* **1994**, *77*, 385.

(54) Marinopoulos, A. G.; Nufer, S.; Elsässer, C. *Phys. Rev. B* **2001**, *63*, 165112.

(55) Hass, K. C.; Schneider, W. F.; Curioni, A.; Andreoni, W. *Science* **1998**, *282*, 265.

(56) Hass, K. C.; Schneider, W. F.; Curioni, A.; Andreoni, W. *J. Phys. Chem. B* **2000**, *104*, 5527.

(57) McHale, J. M.; Navrotsky, A.; Perrotta, A. J. *J. Phys. Chem. B* **1997**, *101*, 603.

(58) Wang, X.-G.; Chaka, A.; Scheffler, M. *Phys. Rev. Lett.* **2000**, *84*, 3650.

(59) Łodziana, Z.; Nørskov, J. K.; Stoltze, P. *J. Chem. Phys.* **2003**, *118*, 11179.

(60) Hohenberg, P.; Kohn, W. *Phys. Rev.* **1964**, *136*, B864.

(61) Kohn, W.; Sham, L. J. *Phys. Rev.* **1965**, *140*, A1133.

(62) Kresse, G.; Hafner, J. *Phys. Rev. B* **1993**, *48*, 13115.

(63) Kresse, G.; Furthmüller, J. *Phys. Rev. B* **1996**, *54*, 11169.

(64) Kresse, G.; Furthmüller, J. *Comput. Mater. Sci.* **1996**, *6*, 15.

(65) Perdew, J. P.; Burke, K.; Ernzerhof, M. *Phys. Rev. Lett.* **1996**, *77*, 3865.

(66) Blöchl, P. E. *Phys. Rev. B* **1994**, *50*, 17953.

(67) Kresse, G.; Joubert, D. *Phys. Rev. B* **1999**, *59*, 1758.

(68) Monkhorst, H. J.; Pack, J. D. *Phys. Rev. B* **1976**, *13*, 5188.

(69) Blöchl, P. E.; Jepsen, O.; Andersen, O. K. *Phys. Rev. B* **1994**, *49*, 16223.

(70) Wyckoff, R. W. G. *Crystal Structures,* 2nd ed.; Wiley-Interscience: New York, 1964.

(71) Murnaghan, F. D. *Proc. Natl. Acad. Sci. U.S.A.* **1944**, *30*, 244.

(72) d'Amour, H.; Schiferl, D.; Denner, W.; Schultz, H.; Holzapfel, W. B. *J. Appl. Phys.* **1978**, *49*, 4411.

(73) French, R. H. *J. Am. Ceram. Soc.* **1990**, *73*, 477.

(74) Holm, B.; Ahuja, R.; Yourdshahyan, Y.; Johanson, B.; Lundqvist, B. I. *Phys. Rev. B* **1999**, *59*, 12777.

(75) *CRC Handbook of Chemistry and Physics,* 83rd ed.; Lide, D. R., Ed.; CRC Press: Boca Raton, FL, 2002.

(76) Kresse, G.; Furthmüller, J. *VASP the Guide.* Available from http://cms.mip.univie.ac.at/VASP (accessed December, 2006).

(77) Jarvis, E. A. A.; Carter, E. A. *J. Phys. Chem. B* **2001**, *150*, 4045.

(78) Łodziana, Z.; Nørskov, J. K.; *J. Chem. Phys.* **2001**, *115*, 11261.

(79) Ruberto, C.; Yourdshahyan, T.; Lundqvist, B. I. *Phys. Rev. B* **2003**, *67*, 195412.

(80) Carrasco, J.; Gomes, J. R. B.; Illas, F. *Phys. Rev. B* **2004**, *69*, 064116.

(81) Alavi, S.; Sorescu, D. C.; Thompson, D. L. *J. Phys. Chem. B* **2003**, *107*, 186.

(82) Sousa, C.; Illas, F.; Paccioni, G. *J. Chem. Phys.* **1993**, *99*, 6818.

(83) Hernández, N. C.; Graciani, J.; Márquez, A.; Sanz, J. F. *Surf. Sci.* **2005**, *575*, 189.

(84) Hernández, N. C.; Sanz, J. F. *J. Phys. Chem. B* **2002**, *106*, 11495.

(85) Borck, Ø.; Schröder, E. *J. Phys.: Condens. Matter* **2006**, *18*, 1.

(86) Wallin, E.; Andersson, J. M.; Münger, E. P.; Chirita, V.; Helmersson, U. *Phys. Rev. B* **2006**, *74*, 125409.

(87) Lewis, J.; Schwarzenbach, D.; Flack, H. D. *Acta Crystallogr., Sect. A* **1982**, *A38*, 733.

(88) Xu, Y.-N.; Ching, W. Y. *Phys. Rev. B* **1991**, *43*, 4461.

(89) Shannon, R. D. *Acta Crystallogr., Sect. A* **1976**, *A32*, 751.

(90) Humphrey, W.; Dalke, A.; Schulten, K. *J. Mol. Graphics* **1996**, *14*, 33.

(91) Huber, K. P.; Herzberg, G. *Molecular Spectra and Molecular Structure: Constants of Diatomic Molecules*; Van Nostrand Reinhold: New York, 1979.

(92) Jarvis, E. A.; Carter, E. A. *Phys. Rev. B* **2002**, *66*, 100103(R).

(93) Jarvis, E. A. A.; Carter, E. A. *J. Phys. Chem. B* **2002**, *106*, 7995.

(94) Hernández, N. C.; Sanz, J. F. *Appl. Surf. Sci.* **2004**, *238*, 228.

(95) Sanz, J. F.; Hernández, N. C.; *Phys. Rev. Lett.* **2005**, *94*, 016104.

(96) Yang, R.; Rendell, A. P. *J. Phys. Chem. B* **2006**, *110*, 9608.

(97) Oppenheim, J. N.; Hinnemann, B.; Carter, E. A. Princeton University, Princeton, NJ. Unpublished work.

(98) Rosén, J.; Schneider, J. M.; Larsson, K. *J. Phys. Chem. B* **2004**, *108*, 19320.

(99) Rosén, J.; Schneider, J. M.; Larsson, K. *Solid State Comm.* **2005**, *135*, 90.

(100) Saiz, E.; Cannon, R. M.; Tomsia, A. P. *Acta Mater.* **1999**, *47*, 4209.

(101) Chatain, D.; Coudurier, L.; Eustathopoulos, N. *Rev. Phys. Appl.* **1988**, *23*, 1055.

(102) Merlin, V.; Eustathopoulos, N. *J. Mater. Sci.* **1995**, *30*, 3619.

(103) Lipkin, D. M.; Israelachvili, J. N.; Clarke, D. R. *Philos. Mag. A* **1997**, *76*, 715.

(104) Smith, J. R.; Zhang, W. *Acta Mater.* **2000**, *48*, 4395.

(105) Siegel, D. J.; Hector, L. G., Jr.; Adams, J. B. *Phys. Rev. B* **2002**, *65*, 085415.

(106) Bogicevic, A.; Jennison, D. R. *Phys. Rev. Lett.* **1999**, *82*, 4050.

(107) Foster, A. S.; Lopez Gejo, F.; Shluger, A. L.; Nieminen, R. M. *Phys. Rev. B* **2002**, *65*, 174117.

(108) Xu, Y.-N.; Gu, Z.-Q.; Ching, W. Y. *Phys. Rev. B* **1997**, *56*, 15219.

(109) Wilk, G. D.; Wallace, R. M.; Anthony, J. M. *Appl. Phys. Lett.* **1999**, *74*, 2854.

(110) Rivanenkov, V. V.; Nasluzov, V. A.; Shor, A. M.; Neyman, K. M.; Rösch, N. *Surf. Sci.* **2003**, *525*, 173.

(111) Nasluzov, V. A.; Rivanenkov, V. V.; Shor, A. M.; Neyman, K. M.; Rösch, N. *Chem. Phys. Lett.* **2003**, *374*, 487.

(112) Gomes, J. R. B.; Illas, F.; Cruz Hernández, N.; Márquez, A.; Sanz, J. F. *Phys. Rev. B* **200**2, *65*, 125414.

(113) Gomes, J. R. B.; Illas, F.; Cruz Hernández, N.; Sanz, J. F.; Wander, A.; Harrison, N. M. *J. Chem. Phys.* **2002**, *116*, 1684.

(114) Gomes, J. R. B.; Łodziana, Z.; Illas, F.; *J. Phys. Chem. B* **2003**, *107*, 6411.

(115) Gomes, J. R. B.; Illas, F.; Silvi, B. *Chem. Phys. Lett.* **2004**, *388*, 132.

(116) Topsøe, H.; Clausen, B. S.; Massoth, F. E. In *Hydrotreating Catalysis − Science and Technology*; Anderson, J. R., Boudard, M., Eds.; Springer-Verlag: Berlin, 1996; Vol. 11.

(117) Arrouvel, C.; Tolhoat, H.; Breysse, M.; Raybaud, P.; *J. Catal.* **2004**, *226*, 260.

(118) Carling, K. M.; Glover, W.; Gunaydin, H.; Mitchell, T. A.; Carter, E. A. *Surf. Sci.* **2006**, *600*, 2079.

(119) Carling, K. M.; Carter, E. A. *Acta Mater.* in press.

(120) Pint, B. A. *Surf. Coat. Technol.* **2004**, *188–189*, 71.

(121) Marino, K. A.; Carter, E. A. Princeton University, Princeton, NJ. Unpublished work.